Nonlinear rheology control on early lunar mantle cumulate overturn

Shuoran Yu [1], Nicola Tosi [2,3], Falko Schulz [2,3], Sabrina Schwinger [2], Sebastiano Padovan [2], Doris Breuer [2], Long Xiao [1,4]

[1]State Key Laboratory of Lunar and Planetary Sciences, Macau University of Science and Technology, Macau SAR, China

[2]Institute of Planetary Research, German Aerospace Center (DLR), Berlin, Germany

[3]Department of Astronomy and Astrophysics, Technische Universität Berlin, Berlin, Germany

[4]Planetary Science Institute, China University of Geosciences, Wuhan, China

Key Points:

- We modelled the lunar mantle cumulate overturn using linear diffusion and nonlinear dislocation creep rheologies.
- Whether or not dislocation creep can facilitate the overturn depends on the rheological mixing model.
- Initial velocity and thickness of ilmenite-bearing cumulates can significantly affect the dynamics of overturn.

Corresponding author: S. Yu, shuoran.yu@icloud.com

Abstract

The overturn of mantle cumulates following the crystallization of the lunar magma ocean – particularly the sinking of ilmenite-bearing cumulates (IBC) – provides an explanation for several aspects of the Moon's evolution. However, the growth of a stagnant lid due to the temperature dependence of the viscosity tends to prevent IBC from sinking. Here, we investigate the dynamics of the overturn based on a composition-dependent rheology coupling diffusion and dislocation creep of major lunar mantle minerals via three alternative mixing models: isostrain, isostress and Minimized Power Geometric (MPG). The pre-overturn structure is obtained from a fractional crystallization model of the lunar magma ocean, which predicts the formation of a 36-km-thick IBC layer. The possibility of overturning this layer strongly depends on the choice of the rheological mixing model. The isostress model allows for a rapid and complete overturn, while the isostrain and the experiment-based MPG models do not allow IBC to sink. If IBC started sinking and mixing with the underlying mantle during magma ocean solidification, IBC could be initially distributed across a layer with a thickness of up to 150 km, whose partial overturn is always possible, independent of the rheological model. These results highlight the importance of improving rheological models for relevant lunar materials. In all cases, the overturn occurs via small-scale instabilities.

1 Introduction

The sinking of ilmenite-bearing cumulates (IBC) associated with the so-called lunar mantle cumulate overturn following the crystallization of the lunar magma ocean provides a suitable explanation for the volcanism on the lunar nearside [*Zhong et al.*, 2000; *Zhang et al.*, 2013], the magnetic field anomaly between 4.3 and 3.6 Ga [*Stegman et al.*, 2003; *Shea and Fuller*, 2012], and the present-day low-viscosity zone in the deep lunar mantle [*Weber et al.*, 2011; *Harada et al.*, 2014; *Zhao et al.*, 2019]. However, the crystallised IBC can be entrapped by the growing stagnant lid, i.e. the cold and sluggish layer on the top of lunar mantle [*Elkins-Tanton et al.*, 2002]. The sinking of IBC is possible only in the presence of factors acting to weaken the rheology [*Zhao et al.*, 2019; *Li et al.*, 2019; *Yu et al.*, 2019].

The rheology of mantle materials depends on the styles of their deformation, which can occur via two main mechanisms: diffusion and dislocation creep. Diffusion creep takes place via migration of vacancies in the crystal lattice, causing a linear relation be-

tween stress and strain rate. In contrast, dislocation creep takes place via the migration of imperfect structures in the crystal lattice, resulting in a non-linear relation between stress and strain rate. In our previous work, we assessed the rheological conditions needed to induce the overturn by using the Arrhenius law of diffusion creep [*Yu et al.*, 2019]. We found that the overturn needs a reference viscosity, defined as the viscosity of the lunar mantle at 1600 K, equal to or lower than 10^{20} Pa s. Additionally, for a reference viscosity of 10^{20} Pa s, the overturn requires an activation energy as low as 100 kJ/mol [*Yu et al.*, 2019]. When compared with a standard rheology adopted for lunar mantle materials, i.e. an olivine-dominated composition, an extremely low water content, a grain size of $\sim$ 1 cm [*Nimmo et al.*, 2012] and the low pressure in the lunar mantle, giving rise to an activation energy of 300–400 kJ/mol in the diffusion creep regime and a reference viscosity of $\sim$ 10^{20}–10^{21} Pa s [*Karato and Wu*, 1993; *Hirth and Kohlstedt*, 2003], these results indicate that the overturn requires a weaker and less temperature-dependent mantle rheology [*Yu et al.*, 2019]. These findings are also in line with those of *Zhao et al.* [2019], who suggested that, for an entirely solidified lunar mantle, the overturn requires a low activation energy of about 100 kJ/mol.

The weak mantle rheology needed for the overturn may imply the necessity of dislocation creep to initiate the overturn. Contrary to diffusion creep, the relation between stress and strain in dislocation creep is non-linear, resulting in an effective viscosity that depends on both temperature and stress [e.g., *Schubert et al.*, 2001]. Thus, there is a positive feedback between the mobility of mantle materials and a decrease in their viscosity. Such feedback is more effective at shallow mantle depths, characterized by a temperature of hundreds of degrees. For example, in the Earth, dislocation creep in the shallow mantle allows the gravitational instability of the lithosphere to develop at an initial very low rate, followed by a markedly higher rate near its climax. This dynamic behavior well explains the time interval between lithosphere thickening and lithosphere thinning observed for example in the Tibetan and Aegean regions [e.g. *Houseman and Molnar*, 1997; *Molnar et al.*, 1998]. Similarly, the lunar mantle cumulate overturn may also be facilitated by dislocation creep. It has been noted that the thermal effects of dislocation creep can be mimicked by multiplying the activation energy of dislocation creep by a factor of 0.3–0.5 [*Christensen*, 1984]. Although this finding presents various limitations [*Schulz et al.*, 2020], it may explain the low activation energy required for the overturn [*Yu et al.*, 2019]. The intrinsically weak rheology of ilmenite is another possible factor for producing the weak rheology

needed for the overturn. *Dygert et al.* [2016] experimentally measured the rheological relation for the dislocation creep of ilmenite. For a stress of 1 MPa and an ilmenite content of 8–13 vol. %, the weak rheology of ilmenite can reduce the effective viscosity of IBC by up to three orders of magnitude. Partitioning of strain into the rheologically weak phase has also been found in the sinking of lithosphere [*Dygert et al.*, 2019].

Nevertheless, the effects of dislocation creep and chemical composition on the mantle viscosity are not straightforward and also depend on the rheological mixing model, which determines how stress and strain rate are partitioned among every deformable components. It is thus necessary to examine the effects of rheological mixing models in order to provide a comprehensive picture of the influence of complex rheologies on the cumulate overturn. Furthermore, as we will discuss in the paper, the IBC are not only composed of olivine and ilmenite, but also of clinopyroxene. Thus, a complete analysis of the overturn dynamics also requires a composition-dependent rheology that couples the creep properties of all these major components of the lunar mantle.

According to the theory of Rayleigh-Taylor instability [e.g. *Whitehead*, 1988; *Hess and Parmentier*, 1995], weakening the rheology of the IBC can significantly shorten the time needed for the development of the overturn and increase its characteristic spatial wavelength. *Parmentier et al.* [2002] suggested that for an IBC layer with a thickness of 50 km and a viscosity four-orders-of-magnitude lower than that of the underlying mantle, a hemispherical overturn would occur. This so-called degree-one overturn could explain the focusing of KREEP materials on the lunar nearside [*Haskin et al.*, 1998; *Korotev*, 2000; *Jolliff et al.*, 2000; *Wieczorek and Phillips*, 2000]. In the context of non-linear mantle rheology, there is a positive feedback between the mobility and rheological weakening of the IBC. The question is thus raised whether or not dislocation creep of mafic minerals or ilmenite can influence the overturn and favour the growth of a long-wavelength instability.

With the goal of addressing these questions, in this work we use numerical simulations of thermo-chemical mantle convection to study the problem of the lunar mantle cumulate overturn in the presence of a combination of various linear and non-linear rheologies.

2 Model and Methods

2.1 Conservation Equations

As in *Yu et al.* [2019], we modelled the thermo-compositional overturn based on an initial three-layer structure consisting of crust, IBC and cumulate mantle. To this end, we solved the dimensionless conservation equations of mass (1), linear momentum (2), thermal energy (3), and transport of composition (4) appropriate for solid-state mantle convection, namely:

$$\nabla' \cdot \boldsymbol{u}' = 0\,, \tag{1}$$

$$-\nabla' p' + \nabla' \cdot \left[\eta'_{\mathrm{e}} \left(\nabla' \boldsymbol{u}' + (\nabla' \boldsymbol{u}')^{\mathrm{t}}\right)\right] = \left(RaT' - Ra_C C'\right) g' \hat{e}_r\,, \tag{2}$$

$$\frac{\partial T'}{\partial t'} + \boldsymbol{u}' \cdot \nabla' T' = \nabla^{2'} T' + \frac{Ra_Q}{Ra} Q'(C', t')\,, \tag{3}$$

$$\frac{\partial C'}{\partial t'} + \boldsymbol{u}' \cdot \nabla' C' = 0\,, \tag{4}$$

where the prime indicates non-dimensional operators and variables, $\boldsymbol{u}'$ is the velocity, p' the dynamic pressure, η'_{e} the effective viscosity (see Section 2.2), T' the temperature, C' the composition field, g' a factor controlling the variation of gravitational acceleration with depth (derived below), $\hat{e}_r$ the radial unit vector, t' the time, and $Q'(C', t')$ the composition- and time-dependent heat production rate. The non-dimensional numbers Ra, Ra_C and Ra_Q are the thermal, compositional and internal heating Rayleigh numbers, which are defined in terms of dimensional quantities as follows:

$$Ra = \frac{\alpha \rho_{\mathrm{m}} g_{\mathrm{s}} \Delta T D^3}{\kappa \eta_{\mathrm{r}}}\,, \tag{5}$$

$$Ra_C = \frac{\left(\rho_{\mathrm{IBC}} - \rho_{\mathrm{cr}}\right) g_{\mathrm{s}} D^3}{\kappa \eta_{\mathrm{r}}}\,, \tag{6}$$

$$Ra_Q = \frac{\alpha \rho_{\mathrm{m}}^2 g_{\mathrm{s}} Q^0_{\mathrm{IBC}} D^5}{\kappa K \eta_{\mathrm{r}}}\,, \tag{7}$$

where ρ_m, ρ_{IBC} and ρ_{cr} are the density of the mantle, IBC and crust, α is the coefficient of thermal expansion, g_{s} the gravitational acceleration at the surface, $\Delta T = T_{\mathrm{c}} - T_{\mathrm{s}}$ the initial temperature drop across the mantle (with T_{c} and T_{s} initial core temperature and surface temperature, respectively), D the silicate layer thickness from the surface to the core-mantle boundary (CMB) (i.e. including the crust), κ the thermal diffusivity, K the thermal conductivity, η_{r} the reference viscosity, and Q^0_{IBC} the initial heat production of the IBC layer (see below).

The non-dimensional field variables in eqs. (1) – (4) are obtained by employing the usual scaling factors. The length is scaled with the silicate layer thickness D; the time

with the diffusion timescale D^2/κ; the velocity with κ/D; the pressure with $\eta_r\kappa/D^2$; the temperature with the temperature scale ΔT and surface temperature T_s, i.e. $T' = (T - T_s)/\Delta T$. The composition field is defined as

$$C' = \frac{\rho_i - \rho_{cr}}{\rho_{max} - \rho_{cr}}, \tag{8}$$

where ρ_i corresponds to the dimensional density of the crust, IBC or mantle, ρ_{max} the maximum density in the lunar mantle. In eq. (3), the heat production rate Q' is scaled with Q^0_{IBC} and depends on composition and time as follows:

$$Q'(C', t') = \frac{1}{Q^0_{IBC}} \sum_{i=1}^{4} Q^0_i(C') \exp\left(-\frac{\ln 2}{\tau'_i} t'\right), \tag{9}$$

where the index i refers to the four long-lived radiogenic isotopes ^{235}U, ^{238}U, ^{232}Th and ^{40}K, Q^0_i is the corresponding (dimensional) initial specific heat production that is calculated based on the composition C' for the three materials that we considered (crust, IBC and mantle), and τ'_i is the isotope half-life.

Because of the small core radius, the gravitational acceleration in the lunar mantle varies significantly from the CMB to the surface [e.g., *Garcia et al.*, 2011]. Accordingly, we used a radially-dependent gravitational acceleration computed as in *Schubert et al.* [2001]:

$$g(r) = ar + \frac{b}{r^2}. \tag{10}$$

The coefficients a and b are given by

$$a = \frac{g_s R_0^2 - g_c R_c^2}{R_0^3 - R_c^3}, \tag{11}$$

$$b = g_s R_0^2 - a R_0^3, \tag{12}$$

where g_s and g_c are the gravitational acceleration at the surface and CMB, respectively. The non-dimensional factor g' in eq. (2) is thus defined by scaling eq. (10) with g_s, i.e. $g' = g(r)/g_s$.

Table 1 lists the numerical values of the model parameters. We considered a core with a radius of 390 km that is in line with a recent estimate of 384 ± 93 km based on the analysis of lunar laser ranging data [*Viswanathan et al.*, 2019]. The gravitational acceleration at the surface was set to 1.6 m/s^2. With a core density of 7200 kg m^{-3}, the gravitational acceleration at the CMB was estimated to be 0.78 m/s^2.

For the thermal parameters, we adopted standard values typically assumed for olivine. We used a constant thermal conductivity of 4 W m^{-1} K^{-1} and a thermal expansivity of 3×10^{-5} K^{-1} for the entire silicate shell.

2.2 Rheology

In a deforming polyphase rock, diffusion creep and dislocation creep of every component act simultaneously. To estimate the effective viscosity in eq. (2), a rheological mixing model, which determines how strain rate and stress are partitioned among different phases, must be employed. In this section, we discuss three rheological mixing models that we tested: the isostrain mixing model, the isostress mixing model, and the Minimized Power Geometric (MPG) mixing model.

For mantle materials, the general (dimensional) relation between stress and strain rate can be expressed as an Arrhenius relation [e.g., *Hirth and Kohlstedt*, 2003]:

$$\dot{\epsilon}_{II} = A\sigma_{II}^{n} d^{-m} \exp\left(-\frac{E + pV}{RT}\right), \tag{13}$$

where $\dot{\epsilon}_{II}$ is the second invariant of the strain rate tensor, A a pre-factor, σ_{II} the second invariant of the deviatoric stress tensor, d the grain size, n and m the stress and grain size exponents, E the activation energy, V the activation volume, and R the gas constant. As shown by *Yu et al.* [2019], for the Moon, the pressure dependence in eq. (13) has a small influence on the dynamics of the overturn and can be neglected in first approximation. Accordingly, we set $V = 0$. From the constitutive relation $\sigma_{II} = 2\eta\dot{\epsilon}_{II}$, the viscosity of each deformable component can be expressed in terms of the strain rate as

$$\eta_{k,\dot{\epsilon}} = \frac{1}{2A_k^{1/n}} d^{m_k/n_k} \dot{\epsilon}_{II,k}^{(1-n_k)/n_k} \exp\left(\frac{E_k}{n_k RT}\right), \tag{14}$$

or in terms of stress as

$$\eta_{k,\sigma} = \frac{1}{2A_k} d^{m_k} \sigma_{II,k}^{1-n_k} \exp\left(\frac{E_k}{RT}\right), \tag{15}$$

where the subscript k is used to indicate the deformation component, e.g. the dislocation creep of clinopyroxene. For a better comparison with the modelling results in our previous work, we chose the viscosity of olivine (olv) diffusion creep (dif) at reference temperature T_r and reference grain size d_r to be the reference viscosity, i.e.

$$\eta_\mathrm{r} = \frac{1}{2A_{\mathrm{olv,dif}}} d_\mathrm{r}^{m_{\mathrm{olv,dif}}} \exp\left(\frac{E_{\mathrm{olv,dif}}}{RT_\mathrm{r}}\right) \tag{16}$$

166 **Table 1.** Values of model parameters.

Symbol	Parameter	Value
R_0	Moon radius	1740 km
R_c	Core radius	390 km
D_{cr}	Crust thickness	43 km
D_{IBC}	IBC thickness	36 or 150 km
D	Silicate shell thickness	1350 km
α	Thermal expansivity	3×10^{-5} K^{-1}
K	Thermal conductivity	4 W m^{-1} K^{-1}
κ	Thermal diffusivity	10^{-6} m^2 s^{-1}
ρ_{cr}	Crust density	2715 kg m^{-3}
ρ_{IBC}	IBC density	3479–4012 kg m^{-3}
ρ_{max}	Maximum density	4102 kg m^{-3}
ρ_m	Mantle density	3204 kg m^{-3}
ρ_c	Core density	7200 kg m^{-3}
c_c	Core heat capacity	780 J kg^{-1} K^{-1}
g_s	Surface gravity	1.6 m s^{-2}
g_c	CMB gravity	0.78 m s^{-2}
T_s	Surface temperature	250 K
T_c	Initial core temperature	2180 K
T_r	Reference temperature	1600 K
ΔT	Temperature scale	1930 K
Q^0_{cr} (*)	Initial crust heat production	3.11×10^{-10} W kg^{-1}
Q^0_{IBC} (*)	Initial IBC heat production	1.75–4.35 $\times 10^{-11}$ W kg^{-1}
Q^0_m (*)	Initial mantle heat production	2.77×10^{-12} W kg^{-1}

(*) The total initial heat production of the crust, IBC and mantle is given by the sum of the heat productions of the four radiogenic isotopes for each layer at $t = 0$.

By scaling $\eta_{k,\dot{\epsilon}}$ and $\eta_{k,\sigma}$ with $\eta_{\rm r}$, we determined the dimensionless viscosity as

$$\eta'_{k,\dot{\epsilon}} = \gamma_k G^{m_k/n_k} \dot{\epsilon}'^{(1-n_k)/n_k}_{II,k} \exp\left[\frac{E'_k}{n_k\left(T'+T'_0\right)} - \frac{E'_k}{n_k\left(T'_{\rm r}+T'_0\right)}\right], \tag{17}$$

and

$$\eta'_{k,\sigma} = 2^{n_k-1}\gamma_k^{n_k} G^{m_k} \sigma'^{1-n_k}_{II,k} \exp\left(\frac{E'_k}{T'+T'_0} - \frac{E'_k}{T'_{\rm r}+T'_0}\right), \tag{18}$$

where γ_k is a dimensionless pre-factor, $G = d/d_{\rm r}$, $E'_k = E_k/R\Delta T$, $T' = (T-T_0)/\Delta T$, $T'_0 = T_0/\Delta T$, and $T'_{\rm r} = (T_{\rm r}-T_0)/\Delta T$. The pre-factor γ_k is given by

$$\gamma_k = \frac{A_{\rm olv,dif}}{A_k^{1/n_k}} d_{\rm r}^{\left(m_k/n_k - m_{\rm olv,dif}\right)} \left(\frac{\kappa_{\rm r}}{D^2}\right)^{(1-n_k)/n_k} \exp\left(\frac{E_k}{n_k R T_{\rm r}} - \frac{E_{\rm olv,dif}}{R T_{\rm r}}\right). \tag{19}$$

In the isostrain mixing model, every component deforms with the same strain rate and the total stress is partitioned according to the arithmetic average, i.e.

$$\sigma_{II} = \sum_k \phi_k \sigma_{II,k}, \tag{20}$$

where ϕ_k is the volumetric fraction of the mineral associated with the k-th deformable component. By multiplying eq. (20) by $1/2\dot{\epsilon}_{II}$, we can determine the viscosity of the isostrain mixing model as

$$\eta_{\rm isostrain} = \sum_k \phi_k \eta_{k,\dot{\epsilon}}. \tag{21}$$

By scaling $\eta_{\rm isostrain}$ with $\eta_{\rm r}$, we obtain the dimensionless viscosity of the isostrain mixing model, i.e.

$$\eta'_{\rm isostrain} = \sum_k \phi_k \eta'_{k,\dot{\epsilon}}. \tag{22}$$

In the isostress mixing model, every component experiences the same stress and it is the total strain rate to be partitioned according to the arithmetic average, i.e.

$$\dot{\epsilon}_{II} = \sum_k \phi_k \dot{\epsilon}_{II,k}. \tag{23}$$

By multiplying eq. (23) by $2/\sigma_{II}$, the viscosity of isostress mixing model can be determined as

$$\eta_{\rm isostress} = \left(\sum_k \frac{\phi_k}{\eta_{k,\sigma}}\right)^{-1}. \tag{24}$$

Accordingly, the dimensionless effective viscosity for the isostress mixing model is

$$\eta'_{\rm isostress} = \left(\sum_k \frac{\phi_k}{\eta'_{k,\sigma}}\right)^{-1}. \tag{25}$$

The dimensionless total stress needed for estimating $\eta'_{k,\sigma}$ is calculated numerically by solving the equation

$$\dot{\epsilon}'_{II} = \sum_k 2^{-n_k} \phi_k \gamma_k^{-n_k} G^{-m_k} \sigma'^{n_k}_{II} \exp\left[-\left(\frac{E'_k}{T' + T'_0} - \frac{E'_k}{T'_\mathrm{r} + T'_0}\right)\right]. \tag{26}$$

Isostrain and isostress mixing models provide the upper and lower limit to the effective viscosity, respectively. However, the stress and strain rate are usually partitioned among different deformable components and the actual viscosity of a mixture usually lies between these two end members [*Tullis et al.*, 1991]. For this reason, we also considered the MPG mixing model where total stress and total strain rate are partitioned based on a geometric average. This model does not correspond to a specific way with which the stress is applied to the deformable components, but gives an effective viscosity well in agreement with experimental results [*Huet et al.*, 2014]. To derive the effective viscosity of the MPG model, we write the total strain rate as

$$\dot{\epsilon}_{II} = \prod_k \dot{\epsilon}^{\phi_k}_{II,k}. \tag{27}$$

The effective viscosity can be obtained by minimizing the total deformation power

$$P = \sum_k 2\phi_k \eta_{k,\dot{\epsilon}} \dot{\epsilon}^2_{II,k}. \tag{28}$$

Following *Huet et al.* [2014], we can exploit the method of the Lagrange multipliers to minimize P. The effective viscosity of the MPG model can thus be determined as

$$\eta_\mathrm{MPG} = \sum_k \frac{\phi_k n_k}{n_k + 1} \prod_k \left(\eta_{k,\dot{\epsilon}} \frac{n_k + 1}{n_k}\right)^{\frac{\phi_k a_k n_k}{\sum_j \phi_j a_j n_j}}, \tag{29}$$

where $a_k = \prod_{k \neq j} \left(n_j + 1\right)$ and $\eta_{k,\dot{\epsilon}}$ is determined using the total strain rate. Accordingly, the dimensionless form of η_MPG is

$$\eta'_\mathrm{MPG} = \sum_k \frac{\phi_k n_k}{n_k + 1} \prod_k \left(\eta'_{k,\dot{\epsilon}} \frac{n_k + 1}{n_k}\right)^{\frac{\phi_k a_k n_k}{\sum_j \phi_j a_j n_j}}. \tag{30}$$

We also note that MPG mixing model can be derived from the partitioning for either strain rate or stress. For the same bulk composition, both two partitioning schemes yield similar effective viscosity and thus, are equivalent.

The parameter ϕ_k depends on how the distribution of chemical composition varies with the dynamics of the lunar mantle. To consider the time variation of ϕ_k during the overturn, we use the following transport equation:

$$\frac{\partial \phi_k}{\partial t'} + \mathbf{u}' \cdot \nabla \phi_k = 0. \tag{31}$$

Initial profiles of ϕ_k are obtained from the modelling of lunar magma ocean crystallization (see Section 2.3).

We quantify the importance of dislocation creep by computing a factor f that measures the fraction of dislocation-creep component in the effective viscosity. For the three mixing models above, their individual f-factors are defined as

$$f_{\text{isostrain}} = \frac{1}{\eta'_{\text{isostrain}}} \sum_{dis} \phi_k \eta'_{k,\dot{\epsilon}} \,, \tag{32}$$

$$f_{\text{isostress}} = \eta'_{\text{isostress}} \sum_{dis} \frac{\phi_k}{\eta'_{k,\sigma}} \,, \tag{33}$$

and

$$f_{\text{MPG}} = \frac{\sum_{dis} \left| \lg \left(\eta'_{k,\dot{\epsilon}} \frac{n_k + 1}{n_k} \right)^{\frac{\phi_k a_k n_k}{\sum_j \phi_j a_j n_j}} \right|}{\sum_{k} \left| \lg \left(\eta'_{k,\dot{\epsilon}} \frac{n_k + 1}{n_k} \right)^{\frac{\phi_k a_k n_k}{\sum_j \phi_j a_j n_j}} \right|} \,. \tag{34}$$

The symbol $\sum_{dis}$ indicates a sum for the quantities when k specifies dislocation creep components.

As we will discuss in Section 2.3, the IBC layer is composed primarily of olivine, clinopyroxene and ilmenite, whereas the underlying lunar mantle is composed primarily of olivine and orthopyroxene. The rheological parameters of these major components are shown in Table 2. The rheology of orthopyroxene in the diffusion-creep regime is based on the laboratory experiments on the $En_{0.95}Fo_{0.05}$ aggregates [*Tasaka et al.*, 2013]. The diffusion creep of ilmenite has never been measured in laboratory experiments. Instead, we used rheological data of magnetite diffusion-creep [*Till and Moskowitz*, 2013] to estimate the viscosity of ilmenite diffusion-creep because of their similar crystal structures [*Dygert et al.*, 2016].

2.3 Initial conditions

As in *Yu et al.* [2019], we started our dynamical simulations from the time characterizing the solidification of the lunar magma ocean, i.e. $\sim$ 4.38 and $\sim$ 4.42 Ga [e.g. *Boyet et al.*, 2015]. Below, we repeat the modelling strategy, presenting additional details that needs to be considered upon accounting for the compositional dependence of the rheology. We modeled the crystallization of the lunar magma ocean with the software alphaMELTS [*Ghiorso et al.*, 2002; *Smith and Asimow*, 2005]. We computed profiles of density, temperature, and heat production rate to be used as initial conditions for the simulations.

247 **Table 2.** Rheological parameters of olivine, orthopyroxene, clinopyroxene, magnetite and ilmenite.

Component (k)	A_k (s^{-1} μm^{m_k} MPa^{-n_k})	m_k	n_k	E_k (kJ/mol)	References
Olivine diffusion creep	1.59×10^9	3.0	1.0	375	*Hirth and Kohlstedt* [2003]
Olivine dislocation creep	1.10×10^5	0	3.5	530	*Hirth and Kohlstedt* [2003]
Orthopyroxene diffusion creep	1.92×10^4	2.0	1.0	320	*Tasaka et al.* [2013]
Orthopyroxene dislocation creep	6.6×10^{13}	0	3.8	820	*Mackwell* [1991]
Clinopyroxene diffusion creep	1.26×10^{15}	3.0	1.0	560	*Bystricky and Mackwell* [2001]
Clinopyroxene dislocation creep	6.31×10^9	0	4.7	760	*Bystricky and Mackwell* [2001]
Magnetite diffusion creep	19.95	3.0	1.0	188	*Till and Moskowitz* [2013]
Ilmenite dislocation creep	6.36	0	3.0	307	*Dygert et al.* [2016]

256 We assumed the bulk composition of *O'Neill* [1991], but an elevated TiO_2 content of 0.4
257 wt%. The TiO_2 content used here corresponds to its maximum value [*Buck and Toksoez*,
258 1980; *Elkins-Tanton et al.*, 2011; *Morgan et al.*, 1978; *Snyder et al.*, 1992], by which the
259 IBC layer can be thick enough to be properly resolved with our numerical grid. Figure
260 1 shows the initial profiles of density, temperature and heat production rate. We distin-
261 guished the IBC layer from the underlying mantle based on its high density. The model
262 results were simplified compared to the obtained crystallization sequence by introducing
263 a simple three-layer structure consisting of the anorthositic crust with a thickness of 43
264 km, the IBC layer with a thickness of 36 km, and the underlying mantle. Each layer is as-
265 signed a volume-averaged density and heat production rate. For further details concerning
266 the crystallization sequence, we refer the reader to section 3.1 of *Yu et al.* [2019].

273 To determine the effective viscosity, the composition of the IBC and of the under-
274 lying mantle are needed. The average composition of IBC is determined as 41.97 vol.%
275 olivine + 45.16 vol.% clinopyroxene + 10.39 vol.% ilmenite + 2.48 vol.% minor com-
276 ponents (whitelockite, quartz, etc.). The average composition of the mantle below the
277 IBC was determined as 63.41 vol.% olivine + 27.20 vol.% orthopyroxene + 9.20 vol.%
278 clinopyroxene + 0.19 vol.% minor components. When estimating the effective mantle vis-
279 cosity, we just consider the effects of olivine, orthopyroxene, clinopyroxene and ilmenite.
280 The rheologies of minor components are modelled with the rheological data of olivine.

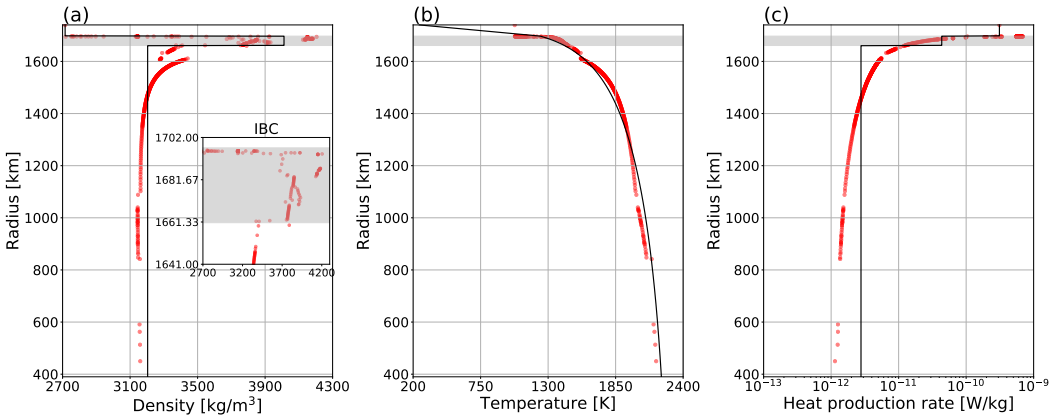

Figure 1. Initial profiles of (a) density, (b) temperature, and (c) heat production rate used as initial conditions for our dynamic models. Red dots correspond to the alphaMELTS calculations, while the black lines indicate the simplified profiles used in the simulations. The gray bar indicates the initial location of the IBC. The density and heat production of each of the three layers are volumetric averages of the values calculated with alphaMELTS. The temperature profile is obtained as a polynomial best-fit of the the alphaMELTS results for the IBC and mantle, which is extended linearly from the base of the crust to the surface.

In general, the thickness of the IBC, which can vary according to different assumptions on the lunar bulk composition, is an important parameter in determining the timing and the dominant wavelength over which the overturn develops [*Hess and Parmentier*, 1995; *Li et al.*, 2019]. By examining the thickness of IBC for different lunar bulk compositions, we found that it is sensitive to the bulk FeO and bulk TiO_2 content, but not to the abundances of other elements. Among different models of the lunar bulk composition (see e.g. Table 1 of *Elkins-Tanton et al.* [2011]), the typical FeO content varies between 7.8 and 13.9 wt.% and the typical TiO_2 content varies between 0.17 and 0.40 wt.%. By considering the possible ranges of FeO and TiO_2, the IBC thickness varies from $\sim$ 8 to $\sim$ 40 km. The IBC thickness estimated from our model is $\sim$ 36 km and thus approaches the above upper limit. According to the theory of Rayleigh-Taylor instability [*Hess and Parmentier*, 1995; *Whitehead*, 1988], $t_{\mathrm{onset}} \propto 1/D_{\mathrm{ibc}}$ and $\lambda \propto D_{\mathrm{ibc}}$, where t_{onset} is the onset time for the overturn, and λ its dominant wavelength. Accordingly, our IBC thickness tends to minimize the onset time and maximize its spatial wavelength.

Some authors also suggested that the sinking of IBC may have taken place while the lunar magma ocean was not completely solidified. Before the end of lunar magma ocean crystallisation, the IBC likely contains interstitial melt and thus has a weak rheology

that can facilitate the overturn through small-scale instablities [*Parmentier and Hess*, 1999; *Maurice et al.*, 2017; *Boukaré et al.*, 2018; *Li et al.*, 2019]. If this process takes place, the solidified IBC layer can eventually be thicker and comprise also materials from the underlying lunar mantle. This in turn can shorten the onset time of the overturn and increase its spatial wavelength [e.g. *Li et al.*, 2019]. A detailed modelling of the overturn in a solidifying lunar magma ocean would require taking into account the details of crystallization and the behaviour of a two-phase fluid, which is technically challenging at present. To mimic this situation, we modelled the overturn of a an IBC layer with an increased thickness of 150 km. Based on the estimation of *Li et al.* [2019], such a value likely represents the highest thickness that the IBC layer can achieve in case small-scale sinking of ilmenite-rich materials begins before the end of magma ocean solidification. Based on volume conservation, the density and heat production rate of the thickened IBC were determined to be 3479 kg/m^3 and 1.75×10^{-11} W/kg, respectively. Accordingly, for the thick IBC we determined the following composition: 56.86 vol.% olivine + 18.89 vol.% orthopyroxene + 20.19 vol.% clinopyroxene + 3.17 vol.% ilmenite + 0.89 vol.% minor components.

2.4 Modelling cases

We only considered the overturn in a dry lunar mantle. Hence, we used the reference grain size (d_r) as unique parameter controlling the reference viscosity as well as the partitioning between grain-size-sensitive diffusion creep and grain-size-independent dislocation creep [*Schulz et al.*, 2020]. We used reference viscosities of 10^{19}, 10^{20} and 10^{21} Pa s, which correspond to grain sizes of 2.6, 5.6 and 12.0 mm, respectively. These values are also consistent with the estimates of *Nimmo et al.* [2012] within a factor of ~ 5.

Accounting for a self-consistent evolution of the grain size [e.g. *Austin and Evans*, 2007; *Rozel et al.*, 2011] could be important to ultimately assess the role of dislocation creep on the overturn. However, due to the lack of constrains on the initial grain size distribution and on the activation parameters for the growth of ilmenite grains, we limited our analysis to simulations employing a uniform and constant grain size. We discuss the potential effects of a variable grain size in Section 5.

By exploiting the distribution of composition presented in Section 2.3, we examined first the effects of dislocation creep on the viscosity of the thin IBC (36 km), the thick IBC (150 km) and the underlying lunar mantle. Figure 2 shows the viscosity of the thin

IBC layer as a function of temperature for different combinations of reference viscosity and mixing model. The viscosity of olivine diffusion creep is shown as a reference. For a strain rate between 10^{-18} and 10^{-10} s^{-1}, the isostrain mixing model always causes a rheologically-strong IBC with respect to the rheology of olivine for a temperature between 1000 and 2000 K. By increasing the strain rate, the viscosity of IBC at high temperature tends to decrease, but cannot be lower than the viscosity of olivine. Isostress mixing model mainly weakens the rheology of IBC at low temperatures. When the strain rate is higher than 10^{-16} s^{-1}, the isostress mixing model can even significantly reduce the viscosity of IBC above 1600 K. With the MPG model, the dislocation-creep components affect the temperature dependence and the whole level of the IBC viscosity. For a given strain rate, there is always a threshold temperature separating a regime of rheological weakening at low temperatures from a regime of rheological strengthening at high temperatures. We also tested the influence of dislocation-creep components on the viscosity of the thick IBC and underlying lunar mantle. As shown in Figures 3 and 4, the trends of viscosity variation are similar to those observed in Figure 2.

Table 3 lists the modelling cases with the corresponding parameters. To facilitate a comparison with our previous work [*Yu et al.*, 2019], we considered two families of rheology: diffusion-creep rheology of dry olivine, which we use as a reference, and a composition-dependent rheology coupling diffusion- and dislocation-creep of olivine, orthopyroxene, clinopyroxene and ilmenite. The importance of dislocation creep is measured by the f-factor defined in eqs. (32), (33), and (34). For the composition-dependent rheology, we tested the isostrain, isostress, and MPG mixing models to couple the rheologies of different components. The postfix "T" in the case names of Table 3 refers to the thickened IBC layer (150 km) introduced in Section 2.3.

2.5 Numerical solution

We solved eqs. (1)–(4) with our finite-volume code GAIA [*Hüttig et al.*, 2013] in a 1/4-cylindrical geometry because the overturn with complex rheologies requires very small time steps and thus is very time consuming. We employed a constant radial resolution of 4.5 km while the lateral resolution varies from 3 km at the inner boundary to about 14 km at the outer boundary. Such a high resolution is necessary to accurately track the evolution of the thin IBC layer. We initiated the simulations by adding a 1% random noise onto

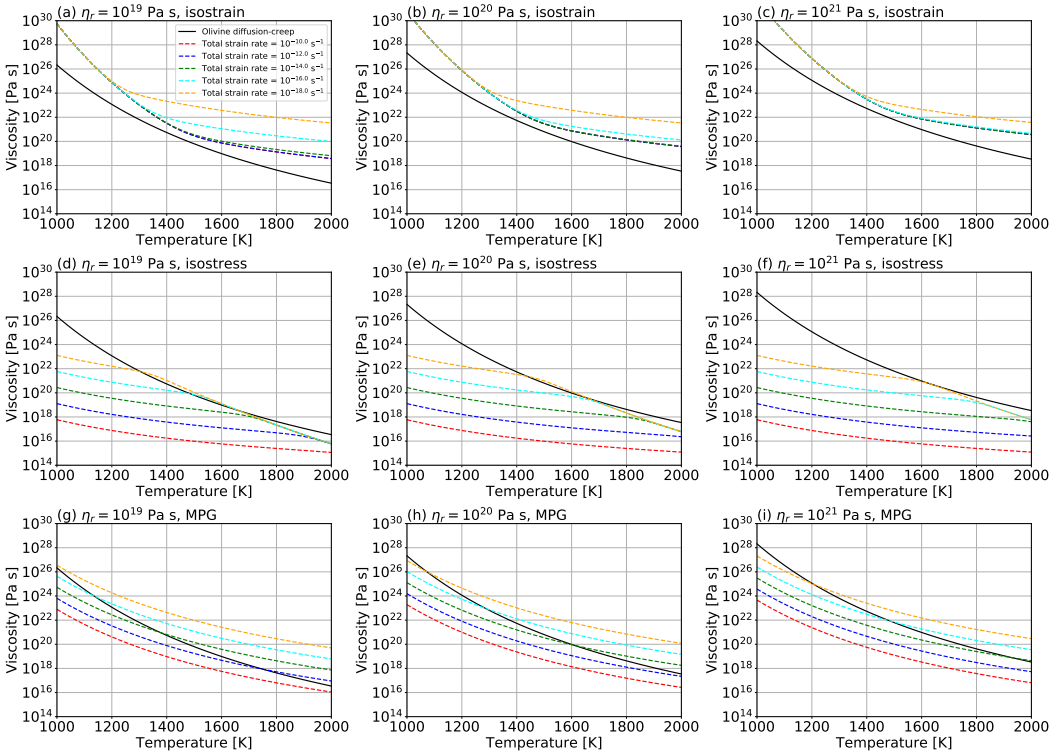

Figure 2. Viscosity of the 36-km-thick IBC layer (41.97 vol.% olivine, 45.16 vol.% clinopyroxene, 10.39 vol.% ilmenite, 2.48 vol.% spinel) as a function of temperature for different reference viscosities η_r obtained with the isostrain (a–c), isostress (d–f), and MPG (g–i) mixing model.

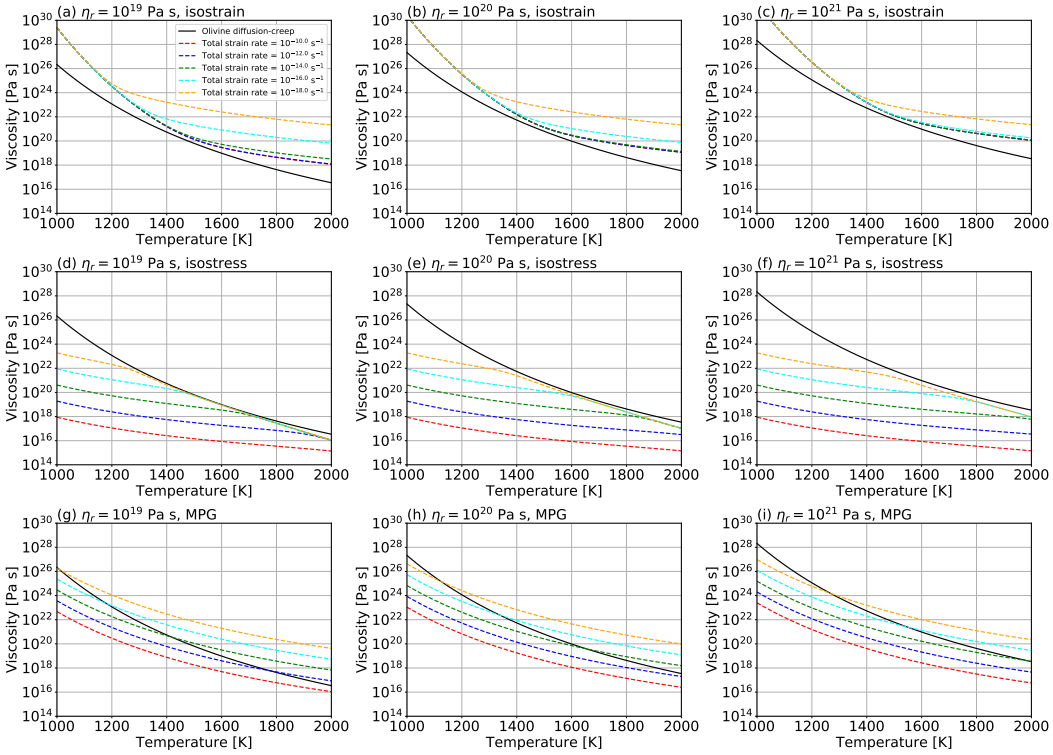

Figure 3. As in Figure 2 but for the 150-km-thick IBC layer (56.86 vol.% olivine, 18.89 vol.% orthopyroxene, 20.19 vol.% clinopyroxene, 3.17 vol.% ilmenite, 0.88 vol.% minor components).

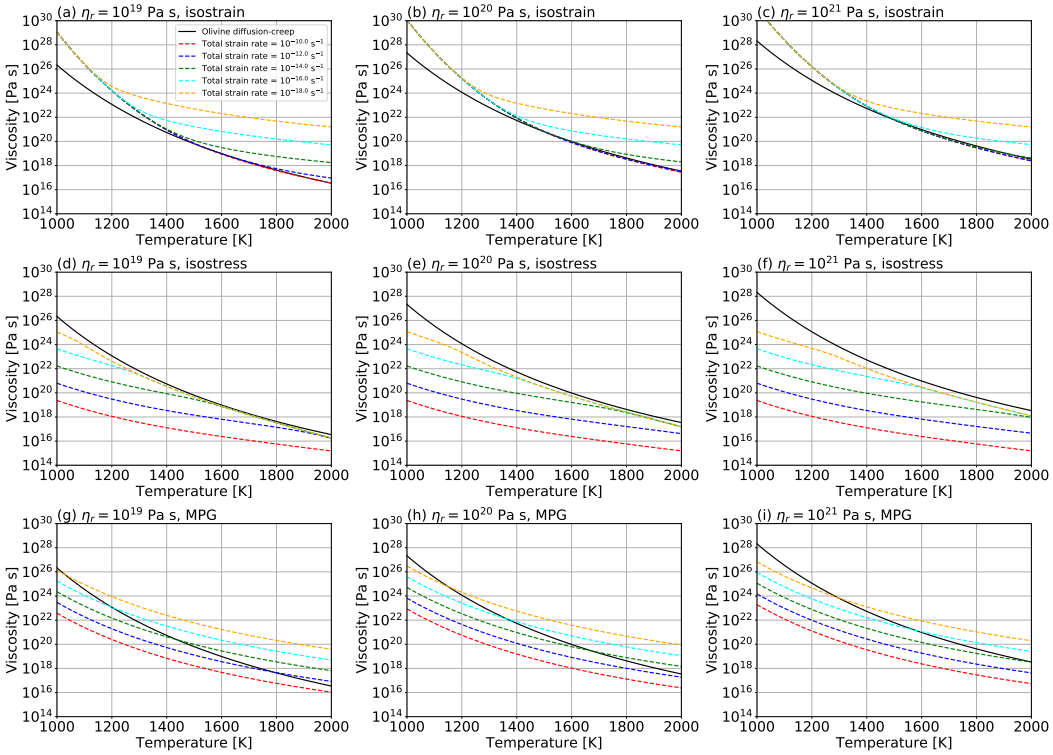

Figure 4. Viscosity of the mantle underlying the IBC layer (63.41 vol.% olivine, 27.20 vol.% orthopyroxene, 9.20 vol. % clinopyroxene and 0.10 vol. % minor components) as a function of temperature for different reference viscosities obtained with the isostrain (a–c), isostress (d–f), and MPG (g–i) mixing model.

361 **Table 3.** Modeling cases according to IBC layer thickness D_{IBC}, reference grain size d_{r}, which controls the
362 reference viscosity η_{r}, rheology, and mixing model.

Case name	D_{IBC} (km)	d_{r} (mm)	η_{r} (Pa s)	Rheology	Mixing model
dif21	36	12.0	10^{21}	olivine diffusion-creep	–
dif20	36	5.6	10^{20}	olivine diffusion-creep	–
dif19	36	2.6	10^{19}	olivine diffusion-creep	–
dif21T	150	12.0	10^{21}	olivine diffusion-creep	–
dif20T	150	5.6	10^{20}	olivine diffusion-creep	–
dif19T	150	2.6	10^{19}	olivine diffusion-creep	–
compisostrain21	36	12.0	10^{21}	composition-dependent	isostrain
compisostrain20	36	5.6	10^{20}	composition-dependent	isostrain
compisostrain19	36	2.6	10^{19}	composition-dependent	isostrain
compisostress21	36	12.0	10^{21}	composition-dependent	isostress
compisostress20	36	5.6	10^{20}	composition-dependent	isostress
compisostress19	36	2.6	10^{19}	composition-dependent	isostress
compMPG21	36	12.0	10^{21}	composition-dependent	MPG
compMPG20	36	5.6	10^{20}	composition-dependent	MPG
compMPG19	36	2.6	10^{19}	composition-dependent	MPG
compisostrain21T	150	12.0	10^{21}	composition-dependent	isostrain
compisostrain20T	150	5.6	10^{20}	composition-dependent	isostrain
compisostrain19T	150	2.6	10^{19}	composition-dependent	isostrain
compMPG21T	150	12.0	10^{21}	composition-dependent	MPG
compMPG20T	150	5.6	10^{20}	composition-dependent	MPG
compMPG19T	150	2.6	10^{19}	composition-dependent	MPG

370 the temperature field and ran them from $\sim$ 4.42 Ga over a time span of 450 Myr, which
371 corresponds to the pre-Nectarian and Nectarian eras in the lunar history.

372 All domain boundaries were considered to be free-slip and impermeable. In addi-
373 tion, we assumed zero heat flux at the domain's sidewalls. The outer boundary was con-
374 sidered to be isothermal with a fixed temperature of 250 K. The temperature of the in-
375 ner boundary, i.e. the CMB, was modelled according to a standard core-cooling boundary

condition as in *Yu et al.* [2019]. We neglected the release of latent heat and gravitational potential energy upon core solidification because of their insignificant effects during the first 500 Myr of lunar evolution [*Laneuville et al.*, 2014].

We treated the advection of composition (eq. (4)) with Lagrangian particles. In particular, upon solving eq. (2), the compositional buoyancy term was obtained by locally averaging the field C' (defined on particles) around every grid point following the implementation of *Plesa et al.* [2012]. The composition-dependent heat production in eq. (3) as well as the effective viscosity in eq. (2) (for the cases where its composition dependence was considered) were obtained in a similar way.

To track the overturn, we followed the evolution of the volumetric fraction of precipitated IBC, ψ_{IBC}, defined as

$$\psi_{\mathrm{IBC}} = \frac{V_{\mathrm{IBC}} - V_{\mathrm{IBC}}^{\mathrm{SL}}}{V_{\mathrm{IBC}}} \times 100\% \,, \tag{35}$$

where V_{IBC} is the total volume of IBC and $V_{\mathrm{IBC}}^{\mathrm{SL}}$ is the volume of IBC which does not participate in the overturn and remains locked in the stagnant lid. As discussed in detail in *Yu et al.* [2019], ψ_{IBC} provides a robust measure for tracking the overturn that is insensitive to the use of cylindrical or spherical geometry.

In Table 3, we do not consider the sinking of the thick IBC with the isostress mixing model. For this condition, the numerical modelling is always not stable because of the rapidly-mobilizing IBC when the overturn tends to be significant. Alternatively, we just discuss the sinking of IBC with isostress mixing model by using the theory of Rayleigh-Taylor instability in Section 4 and discuss the potential consequences of these cases in Section 5.

At low temperatures, the effective viscosity predicted by Arrhenius-like relationships could be very high. In order to avoid convergence issues, we prevented the viscosity from reaching extreme values by truncating it at an upper limit of 10^{30} Pa s. This value is sufficiently large to ensure that all simulations are well in the stagnant lid regime. We imposed no lower limit to the effective viscosity, which was free to decrease as required by the local composition, temperature, and strain rate.

3 Results

Figure 5 shows the time evolution of the fraction of overturned IBC (ψ_{IBC} as defined in eq. (35)) for all modelling cases. The reference viscosity η_{r} affects both the extent and duration of the overturn: the lower η_{r}, the larger the fraction of IBC that sinks into the mantle and the faster is the overturn. For the diffusion-creep rheology, in line with the results of our previous work, which were all based on linear rheologies [*Yu et al.*, 2019], a reference viscosity of 10^{20}–10^{21} Pa s does not allow the overturn to take place, while a reference viscosity of 10^{19} Pa s allows $\sim$ 82 % IBC to sink downwards (solid green line). Increasing the thickness of IBC increases the fraction of IBC that participates in the overturn: with a reference viscosity of 10^{19}, 10^{20}, and 10^{21} Pa s, $\sim$ 87 %, $\sim$ 70 % and $\sim$ 45 % of the IBC layer can sink downwards, respectively (solid cyan, orange and black lines). The influence of dislocation creep on the overturn depends on the rheological mixing model. For the thin IBC layer, no overturn takes place when using the isostrain and MPG mixing models, while the isostress model leads to a rapid and complete overturn for all three reference viscosities (red, blue and green dotted lines). When considering the thick IBC layer, the isostrain mixing model does not allow the overturn to take place, while the MPG mixing model allows $\sim$ 70 %, $\sim$ 53 % and $\sim$ 25 % IBC to sink downwards after $\sim$ 52, $\sim$ 127 and $\sim$ 374 Myr for the reference viscosities 10^{19}, 10^{20} and 10^{21} Pa s, respectively (black, orange and cyan dashed-dotted lines).

Figure 6 shows the time evolution of the IBC's f-factor for each modelling case with composition-dependent rheology. For the isostrain mixing model (dashed lines), the f-factor of IBC is always one initially and starts to decrease after $\sim$ 100 Myr. The higher the reference viscosity, the more rapidly the f-factor decreases. For the MPG model (dashed-dotted lines), the f-factor of IBC shows initially a stable value followed by a sudden decrease when the overturn takes place. The stable initial f-factor does not depend on the reference viscosity, but varies with the thickness of the IBC layer. For the thin and thick IBC, the initial f-factors are $\sim$ 0.8 and $\sim$ 0.9, respectively. The time at which the sudden decrease of the f-factor occurs depends on the reference viscosity: a lower reference viscosity results in an earlier initiation of the f-factor decrease. For the isostress mixing model (dotted lines), the f-factor shows its climax initially and then, tends to decrease rapidly. The peak value of the IBC's f-factor shows a strong dependence on the reference viscosity. For the reference viscosities 10^{19}, 10^{20} and 10^{21} Pa s, its peak values are $\sim$ 0.4, $\sim$ 0.7 and $\sim$ 0.9, respectively.

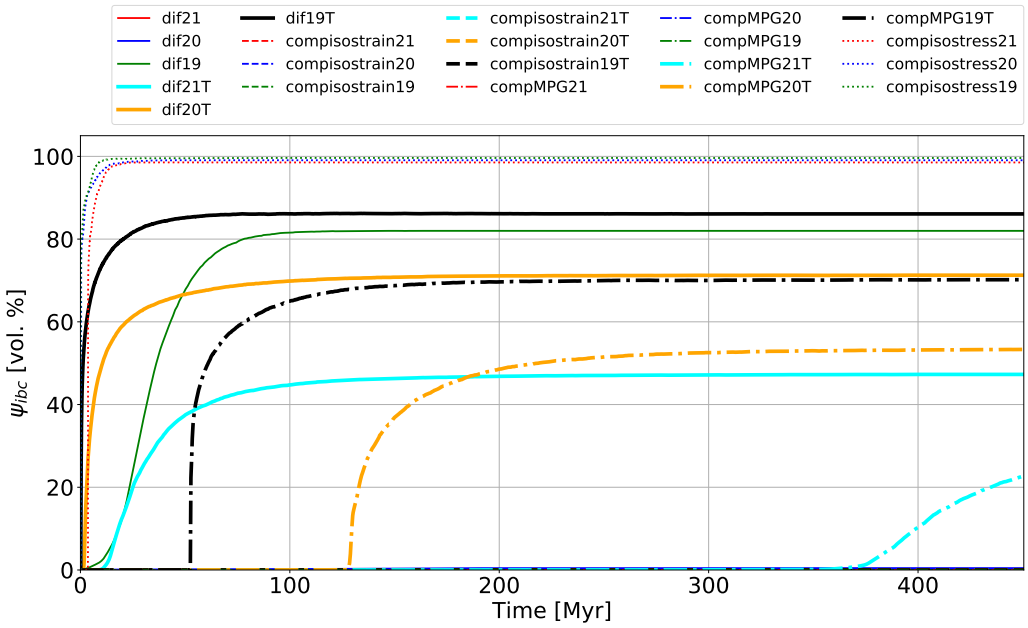

436 **Figure 5.** Time evolution of the volumetric fraction of precipitated IBC (ψ_{IBC} as defined in eq. (35)) for all
437 modeling cases listed in Table 3.

;

441 The time evolution of ψ_{IBC} and of the IBC's f-factor suggests that the influence of
442 dislocation creep on the overturn is much more complex than what we anticipated in our
443 previous work [*Yu et al.*, 2019]. To achieve a better insight into the modelling results, Fig-
444 ure 7 shows the time evolution of the viscosity (left panels), strain rate (central panels)
445 and temperature (right panels) sampled at the original position of IBC for all the mod-
446 elling cases. Here the viscosity, strain rate and temperature of IBC are obtained by aver-
447 aging volumetrically those quantities at the original position of IBC. For the cases dif21,
448 dif20, dif21T and dif20T, the viscosity of IBC keeps increasing with a decreasing rate.
449 In the cases dif19 and dif19T, the viscosity of IBC shows an initial increase, but turns to
450 decrease around $\sim$ 10 and $\sim$ 20 Myr respectively, which correspond to the onset of over-
451 turn, due to the intrusion of underlying hot mantle materials when the IBC sinks. For the
452 isostrain mixing model, the viscosity of IBC shows a very rapid increase over time and
453 at last converges onto the truncation value. Correspondingly, we observe a rapid decrease
454 of strain rate in the IBC, which finally converges to $\sim 10^{-27}$ s^{-1}. Such a low strain rate
455 implies a very weak mobility of IBC. The IBC temperature decreases over time obey-
456 ing the same path due to the dominance of heat conduction in the IBC. The low strain

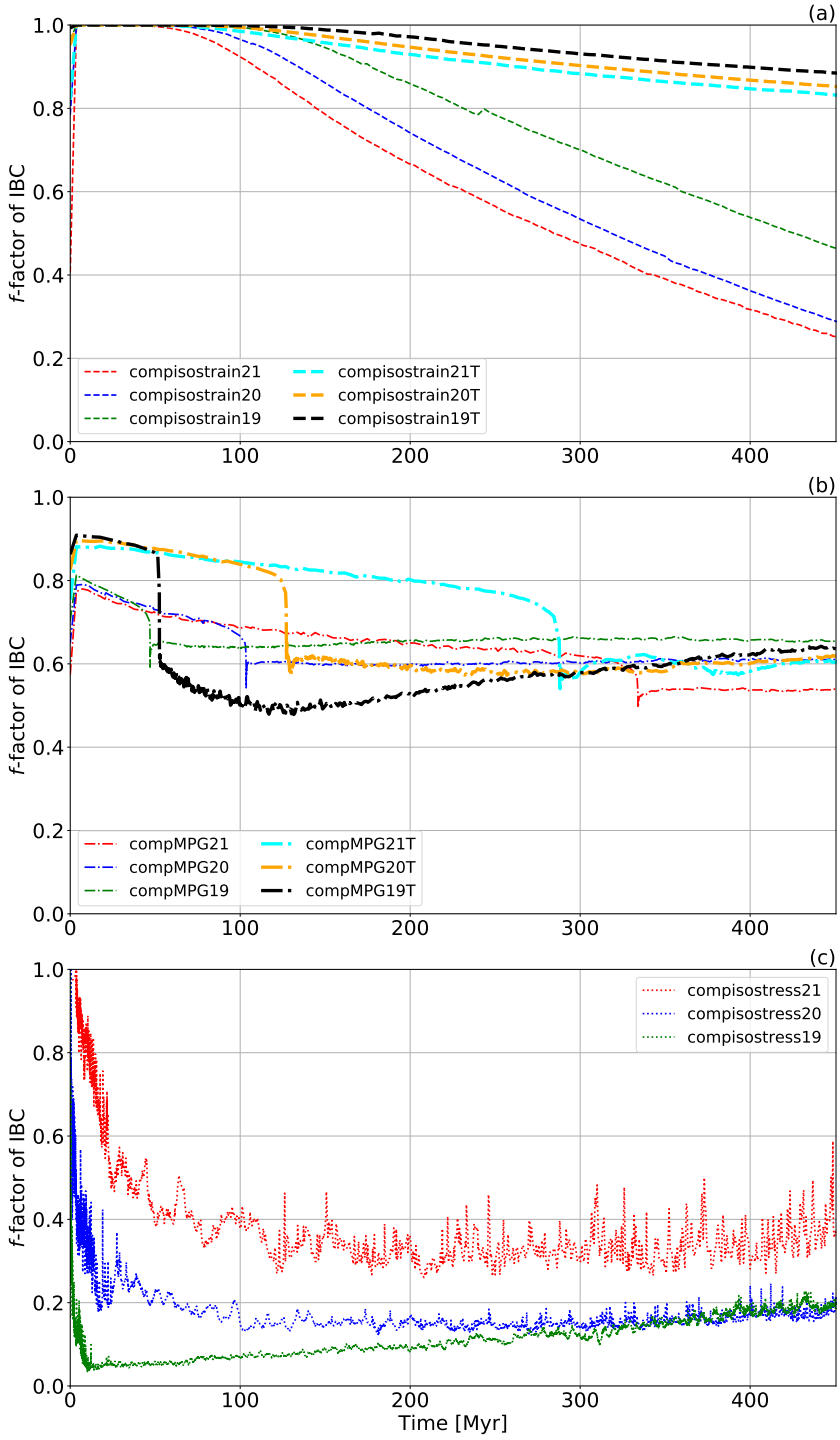

Figure 6. Time evolution of the average f-factor sampled at the original position of IBC for isostrain cases (a), MPG cases (b) and isostress cases (c) shown in Table 3. Here $f = 0$ and $f = 1$ correspond to diffusion-creep-dominated and dislocation-creep-dominated rheology, respectively.

rate of IBC also accounts for the fact that the f-factor equals one only at the beginning of the simulation. For the isostrain mixing model, the rheology of IBC is dominated by the strongest component. Because the viscosity of dislocation creep is proportional to $\dot{\epsilon}^{(1-n)/n}$ and $n > 1$, the low strain rate of IBC can significantly increase the viscosity of dislocation creep components and, in turn, results in the initial dominance of dislocation creep in the IBC. During the subsequent evolution, the decrease of IBC temperature increases the viscosity of the diffusion creep component, which reduces the f-factor of IBC. For the MPG mixing model, the viscosity of IBC shows an initial increase followed by a sudden decrease-increase, and finally tends to be nearly stable over time. For the thin IBC layer, the reference viscosities 10^{19}, 10^{20} and 10^{21} Pa s result in the sudden decrease-increase at $\sim$ 47, $\sim$ 103 and $\sim$ 325 Myr respectively. For the thick IBC, these three reference viscosities result in the sudden decrease-increase at $\sim$ 52, $\sim$ 127 and $\sim$ 287 Myr respectively. Following this trend of viscosity variations, the strain rate of IBC shows a small-scale decrease initially, then experiences a sudden increase of $\sim$ 6 orders of magnitude and a small-scale decrease before finally reaching a stable value. Whether or not the IBC can eventually sink downwards depends on the peak value of the strain rate. For the thin IBC, the peak values of strain rate are $\sim 10^{-17}$, $\sim 10^{-19}$ and $\sim 10^{-20}$ s^{-1} for the reference viscosities 10^{19}, 10^{20} and 10^{21} Pa s, respectively. These strain rates are too low to mobilize the thin IBC. In contrast, in the case of the thick IBC, we observed peak strain rates of $\sim 10^{-12}$, 10^{-13} and 10^{-16} s^{-1} for the same reference viscosities. These three values are high enough to mobilize the IBC. When the overturn takes place, the decrease of the f-factor, or the decline of the importance of dislocation creep in the effective viscosity may account for the cessation of rheological weakening in the IBC. For the isostress mixing model, the viscosity of IBC shows an immediate decrease towards $\sim 10^{18}$ Pa s and accordingly, the strain rate shows a rapid increase towards $\sim 10^{-12}$ s^{-1} at the beginning of the simulations followed by a progressive decrease. The peak strain rate is high enough to allow for a rapid and complete overturn as shown in Figure **??**a. Correspondingly, we observe a rapid increase of temperature because of the intrusion of underlying hot mantle materials.

Since we use a partial cylinder for our simulations, the radial velocity of IBC cannot be easily expanded into a set of orthogonal functions. As a workaround, we obtain the overturn wavelength by simply counting the number of downwellings in snapshots of the composition field, i.e. Figure 8 for compMPGT cases and Figure 10 for compisostress

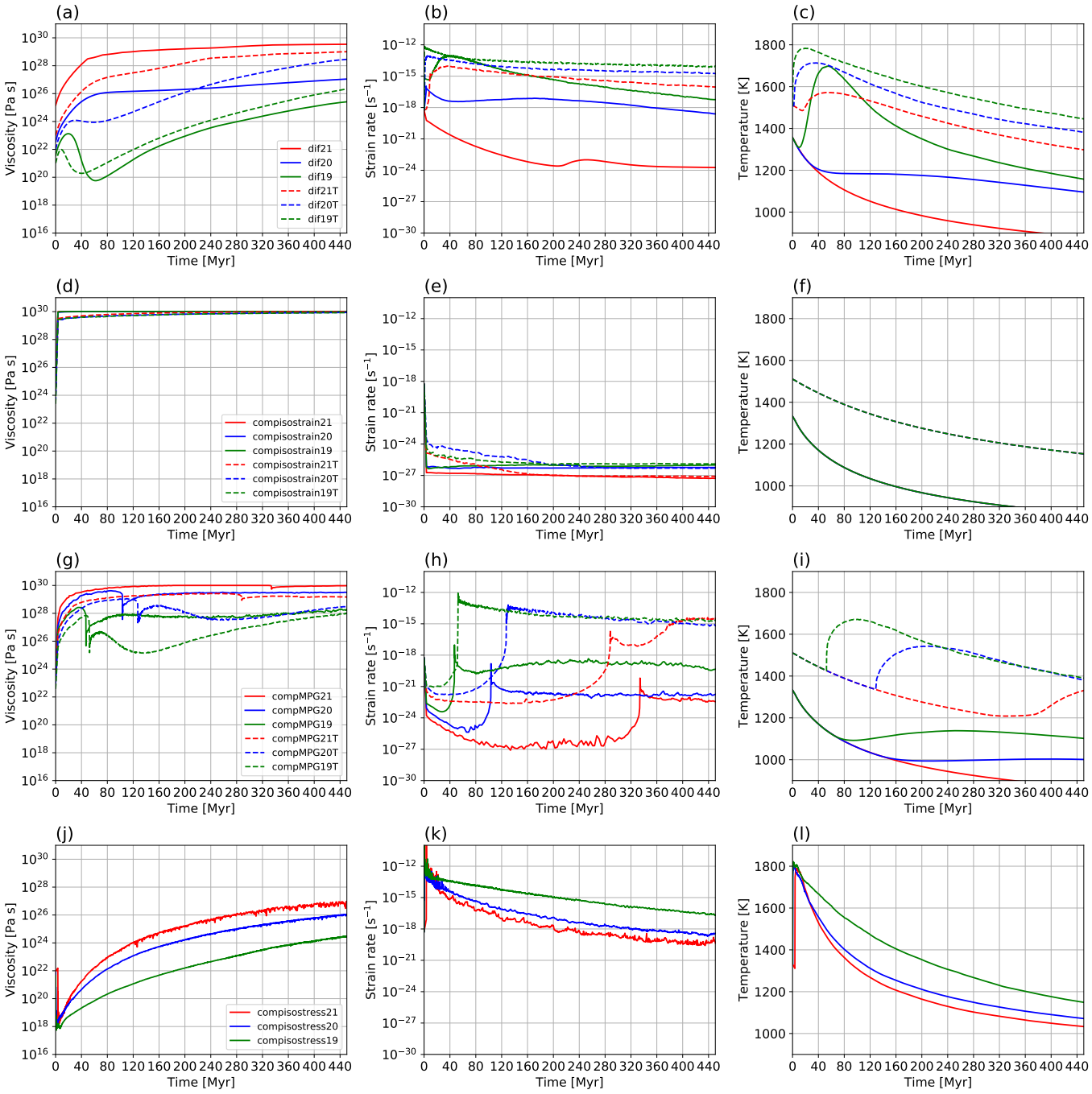

Figure 7. Time evolution of the viscosity (left column), IBC strain rate (middle column) and temperature (right column) sampled at the original position of IBC for the modelling cases with diffusion-creep rheology (a–c), isostrain mixing model (d–f), MPG mixing model (g–i) and isostress mixing model (j–l).

cases. For the case compMPG19T, the overturn initiates with ~ 8 downwellings in 1/4-cylinder at 52 Myr, implying a normalized wavelength (i.e. the overturn wavelength normalized by the perimeter of the Moon) of ~ 0.031. With the development of the overturn, ~ 20 and ~ 32 downwellings are observed at 54 Myr and 56 Myr respectively, indicative of a normalized wavelength of ~ 0.012 and ~ 0.008. In the other two cases, we also observe the overturn developing with a normalized wavelength of ~ 0.03 initially, with the dominant wavelength that tends to decrease over time. Based on the theory of Rayleigh-Taylor instability, the overturn wavelength is proportional to $D_{ibc}\,(\eta_{\mathrm{m}}/\eta_{\mathrm{IBC}})^{1/3}$ where η_{m} and η_{IBC} are the mantle and IBC viscosity, respectively [*Hess and Parmentier*, 1995]. The overturn developing in small-scale diapirs is consistent with the increasing viscosity over radius (see Figure 9), for which the viscosity of IBC is always higher than the viscosity underneath the IBC. The decrease of wavelength over time is a consequence of the decrease of IBC thickness accompanying the overturn.

Figure 10 shows snapshots of chemical composition for the cases compisostress19, compisostress20, and compisostress21. When the overturn begins, we just observe only one thin downwelling in the 1/4 cylinder, which implies a normalized wavelength of ~ 0.25. The overturn developing with a longer wavelength agrees with the fact that the viscosity of IBC is lower than the viscosity below the IBC-mantle boundary by nearly one order of magnitude (see Figure 11). However, this viscosity contrast across the IBC-mantle boundary disappears very rapidly. Together with the decreasing IBC thickness, the overturn soon tends to be governed by tens of small-scale downwellings.

4 Analysis in terms of Rayleigh-Taylor instability

In order to further interpret our results, we examine here the dynamics of the overturn using a simplified model based on the theory of Rayleigh-Taylor instability as we also did in *Yu et al.* [2019]. The downwelling velocity of the unstable IBC-mantle boundary can be expressed as a function of time as

$$w = w_0 \exp\left(\frac{t}{t_{\mathrm{onset}}}\right), \tag{36}$$

where w_0 is the initial velocity and t_{onset} the onset time. The latter depends on the IBC viscosity (η_{IBC}) and on the viscosity at the top of the underlying mantle cumulates (η_{m}) as follows [*Hess and Parmentier*, 1995]:

$$t_{\mathrm{onset}} = \frac{6.5\eta_{\mathrm{m}}^{2/3}\eta_{\mathrm{IBC}}^{1/3}}{(\rho_{\mathrm{IBC}} - \rho_{\mathrm{m}})\, g_{\mathrm{IBC}} D_{\mathrm{IBC}}}, \tag{37}$$

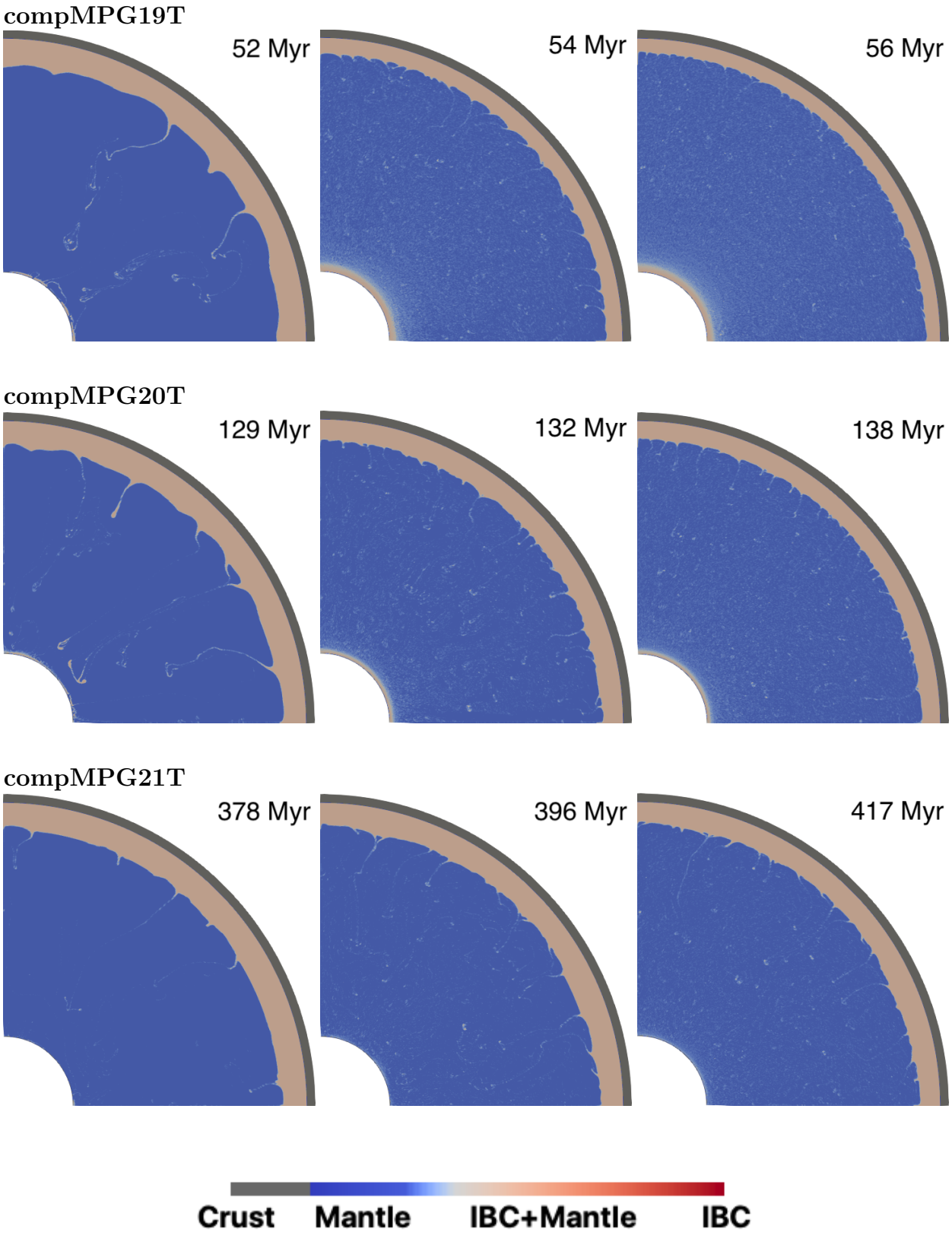

Figure 8. Snapshots of chemical composition for the cases compMPG19T (first line), compMPG20T (second line) and compMPG21T (third line). The gray part indicates the crust, the light brown part the thick IBC layer, and the blue part the underlying mantle.

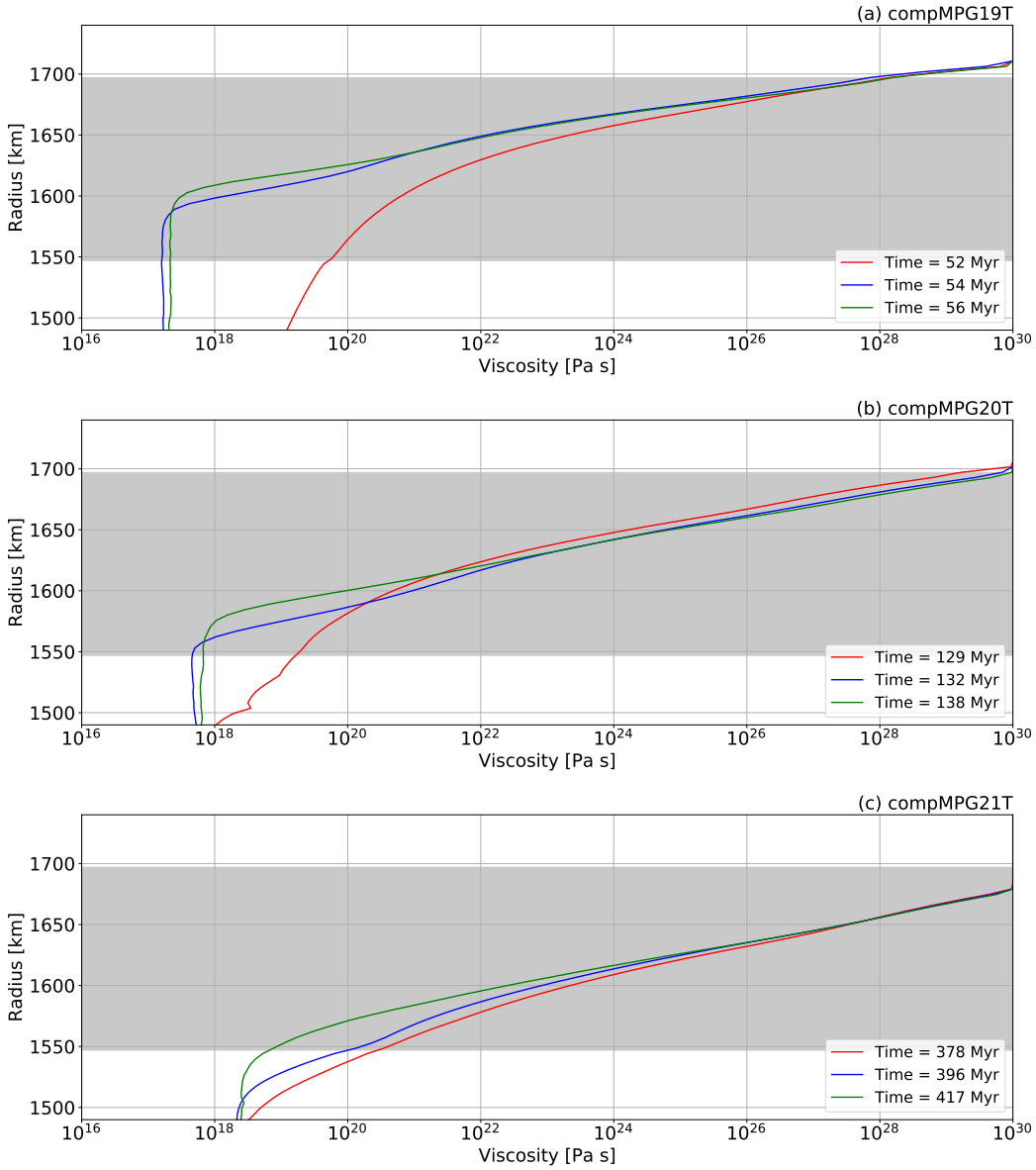

509 **Figure 9.** Viscosity profiles for the shallow mantle at the indicated times for the modelling cases
510 compMPG19T (a), compMPG20T (b) and compMPG21T (c). The gray layer indicates the initial position
511 of the thick IBC.

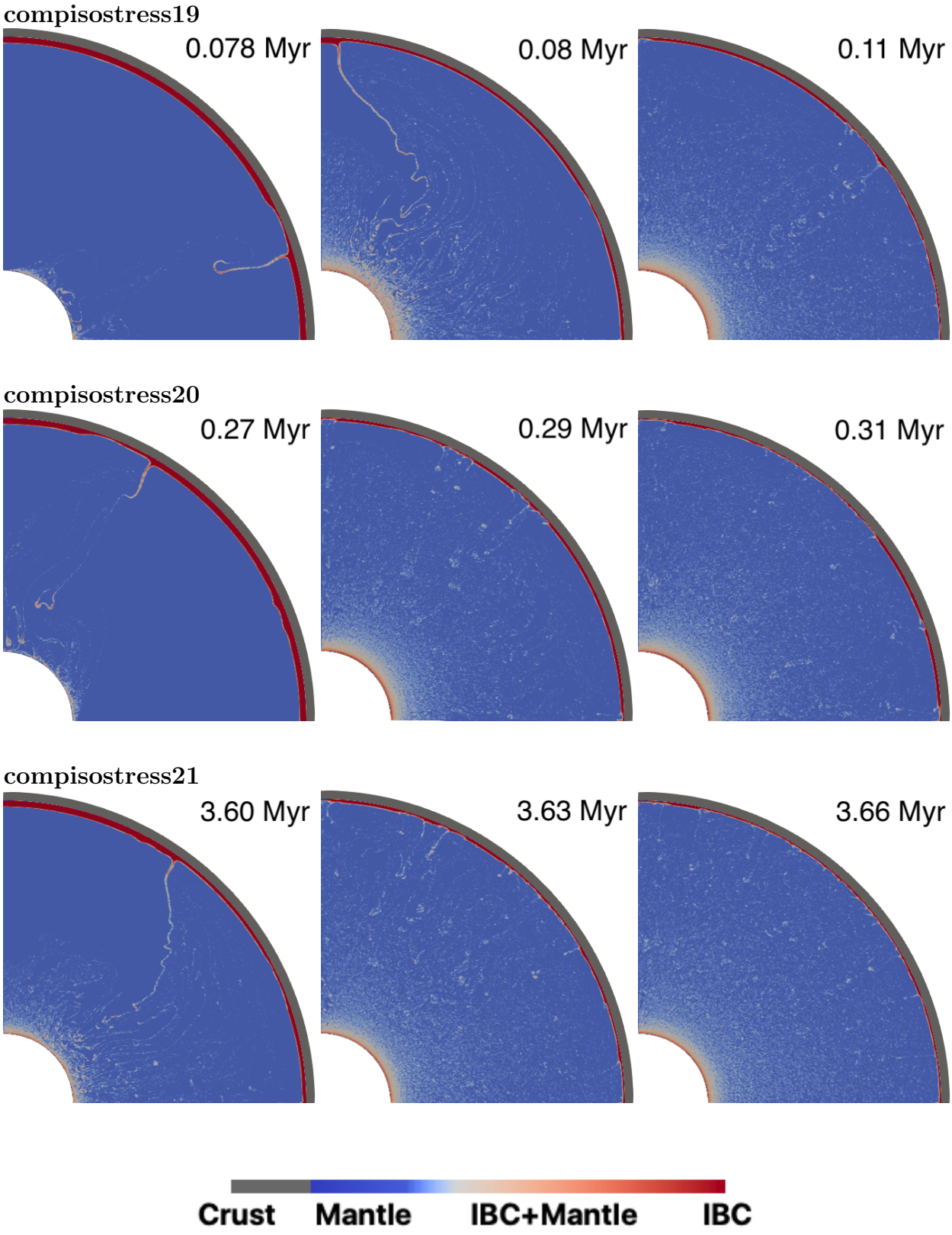

Figure 10. Snapshots of chemical composition for the cases compisostress19 (first line), compisostress20 (second line) and compisostress21 (third line). The gray part indicates the crust, the dark red part the thin IBC layer, and the blue part the underlying mantle.

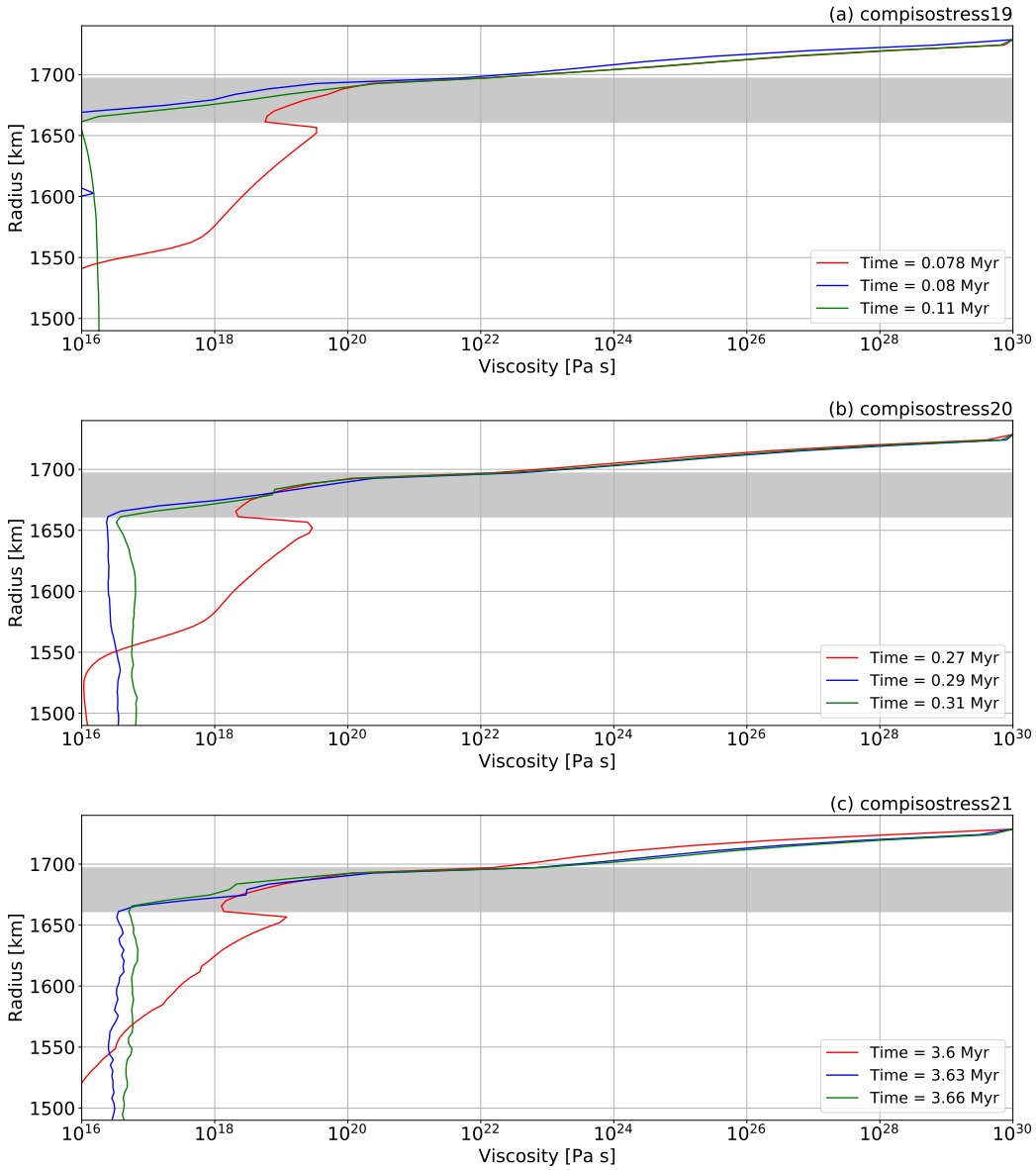

Figure 11. Viscosity profiles for the shallow mantle at the indicated times for the modelling cases compisostress19 (a), compisostress20 (b) and compisostress21 (c). The gray layer specifies the position of the original thin IBC.

where g_{IBC} is the gravitational acceleration at the IBC-mantle boundary. The overturn occurs if $t_{\mathrm{onset}} < t$. We note that the fraction of overturned IBC, i.e. ψ_{IBC}, is proportional to the integral of velocity over time [*Yu et al.*, 2019]. Therefore, the onset time can only be used as an indicator for when the overturn is possible, but not as an indicator for when the finite-amplitude overturn turns to be significant. The overturn wavelength normalized to the lunar perimeter is [*Hess and Parmentier*, 1995]

$$\lambda^* = \frac{2.9 D_{\mathrm{IBC}}}{2\pi R_0} \left(\frac{\eta_{\mathrm{m}}}{\eta_{\mathrm{IBC}}} \right)^{1/3}. \tag{38}$$

To estimate the viscosity associated with dislocation creep, one needs to evaluate the strain rate of the IBC layer and the strain rate at the top of the underlying mantle cumulates, which can be expressed as

$$\dot{\epsilon}_{\mathrm{m}} = \dot{\epsilon}_{\mathrm{IBC}} \approx \frac{w}{D_{\mathrm{IBC}}}. \tag{39}$$

Before the overturn, the temperature in the lunar mantle is largely controlled by heat conduction. As in *Yu et al.* [2019], we solve the heat conduction equation to simulate the evolution of the temperature in the mantle before the onset of the overturn.

In the geodynamic simulations presented above, we considered an initially stationary IBC layer with respect to the underlying mantle cumulates with only a starting small-scale perturbation on the temperature field to induce convection. Hence, the initial velocity of IBC was not explicitly prescribed. Here we consider the initial IBC velocity as a free parameter. We initiated the geodynamic modelling between $\sim$ 4.38 and $\sim$ 4.42 Ga, i.e. the time for the solidification of lunar magma ocean. Hence, the initial velocity of IBC depends on its state in the solidifying lunar magma ocean. If the sinking of IBC could take place before the solidification of lunar magma ocean, the solidified IBC would acquire a high initial velocity that is comparable with the velocity of the fully-developed downwellings. The timescale for the overturn can be expressed as [*Hess and Parmentier*, 1995]

$$t_{\mathrm{overturn}} = \frac{4\pi\eta}{(\rho_{\mathrm{IBC}} - \rho_{\mathrm{m}})\, g D}. \tag{40}$$

Hence, the velocity of the downwelling diapirs reads

$$v_{\mathrm{diapirs}} = \frac{D}{t_{\mathrm{overturn}}} = \frac{(\rho_{\mathrm{IBC}} - \rho_{\mathrm{m}})\, g D^2}{4\pi\eta}. \tag{41}$$

Given $\eta \sim 10^{19}$–10^{21} Pa s, $g \sim 1$ m/s^2, $D \sim 10^6$ m, the typical velocity of the downwelling diapirs is $\sim 10^{-6}$–10^{-4} m/s. We use here 10^{-5} m/s as the initial velocity of IBC if these start sinking before the solidification of the lunar magma ocean is completed. In addition,

we test three values 10^{-10}, 10^{-15} and 10^{-20} m/s for comparison. The initial velocity of 10^{-20} m/s is low enough to characterize a nearly stationary IBC.

We also need to acknowledge two limitations of our simplified model used to constrain the overturn wavelength including the effects of dislocation creep. Firstly, the theory of Rayleigh-Taylor instability is based on the assumption of a small-scale perturbation at the unstable boundary [*Whitehead*, 1988]. Hence, this simplified model is only applicable when t does not greatly exceed t_{onset}. When $t \gg t_{\text{onset}}$, we always observe an extremely high strain rate of IBC caused by a strong increase in the downwelling velocities. The high strain rate and high downwelling velocity can grow to the point of causing a breakdown of the numerical algorithm when solving for the effective viscosity. Besides, the amount of sinking IBC, i.e. ψ_{IBC}, is proportional to the integral of the downwelling velocity over time [*Yu et al.*, 2019]. When t just exceeds t_{onset}, the overturn still needs extra time to become significant. During this time, the downwelling velocity can still increase and in turn, affect the strain rate of IBC. Owing to the approximation based on small-scale perturbation, our simplified model cannot provide any insight into the overturn during this phase. Furthermore, the theory of Rayleigh-Taylor instability as applied here is valid for a 1-D system and thus cannot account for the strain rates associated with the horizontal component of the velocity in the IBC. For this reason, eq. (39) always underestimates the strain rate of IBC. Based on Figures 2–4, the underestimation of strain rate always results in an overestimation of viscosity and correspondingly, an underestimation of overturn wavelength. Because of these two limitations, our simplified model can only provide information on the lower limit of the wavelength when the overturn just initiates. Thus, we can use this model to verify qualitatively the results of the numerical simulations.

As shown in Section 3, the isostrain mixing model does not allow the overturn, independent of the reference viscosity and IBC thickness (see Figure 5). Figure 12 shows the evolution of the onset time and wavelength for the sinking of the thin (36 km) IBC layer according to the simplified model presented above. For all these cases, an increase in the initial downwelling velocity reduces the onset time. Nevertheless the onset time is always greater than the actual time, even for an initial velocity of 10^{-5} m/s. Hence, the overturn is never possible. Figure 13 shows the evolution of the onset time and wavelength for the sinking of the thick (150 km) IBC layer. In this case, the overturn cannot take place unless the initial downwelling velocity increases to 10^{-5} m/s and the reference viscosity decreases to 10^{19} Pa s.

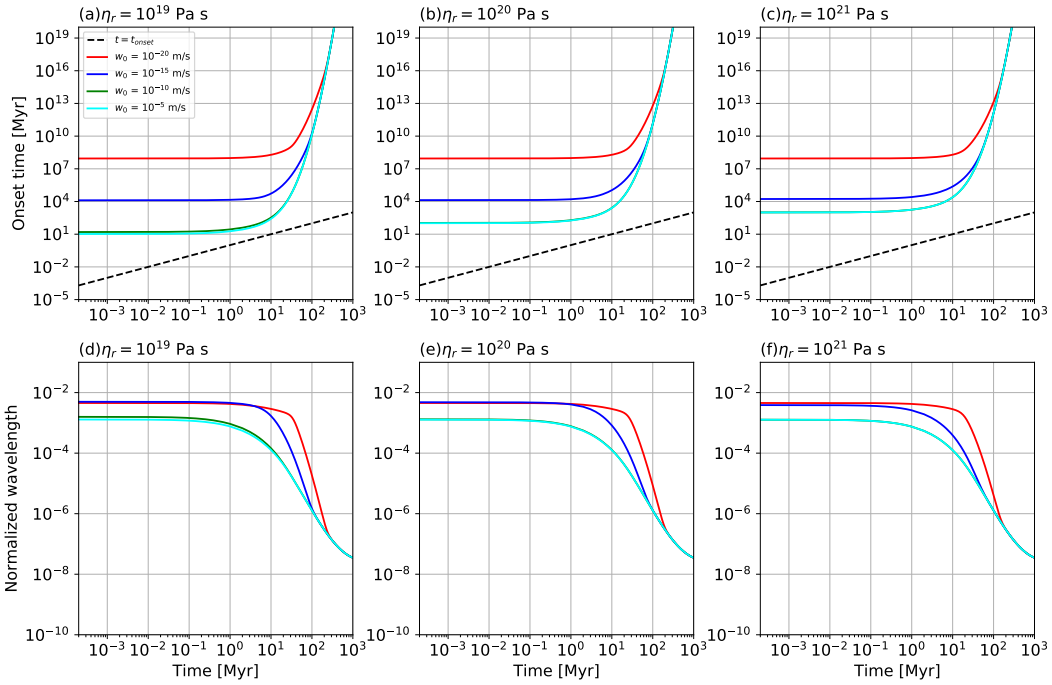

593 **Figure 12.** Time evolution of the onset time (a–c) and wavelength (d–f) for the thin IBC (36 km) based on
594 the isostrain mixing model for different values of the reference viscosities and initial velocities assigned to the
595 IBC-mantle boundary.

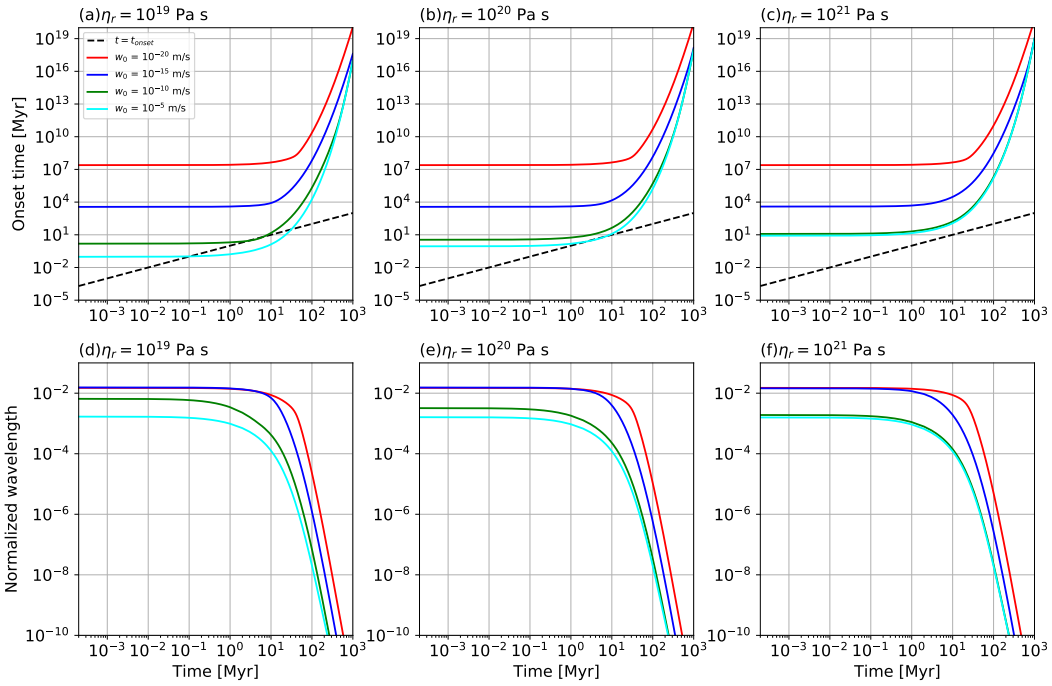

596 **Figure 13.** Time evolution of the onset time (a–c) and wavelength (d–f) for the thick IBC (150 km) based
597 on the isostrain mixing model for different values of the reference viscosities and initial velocities.

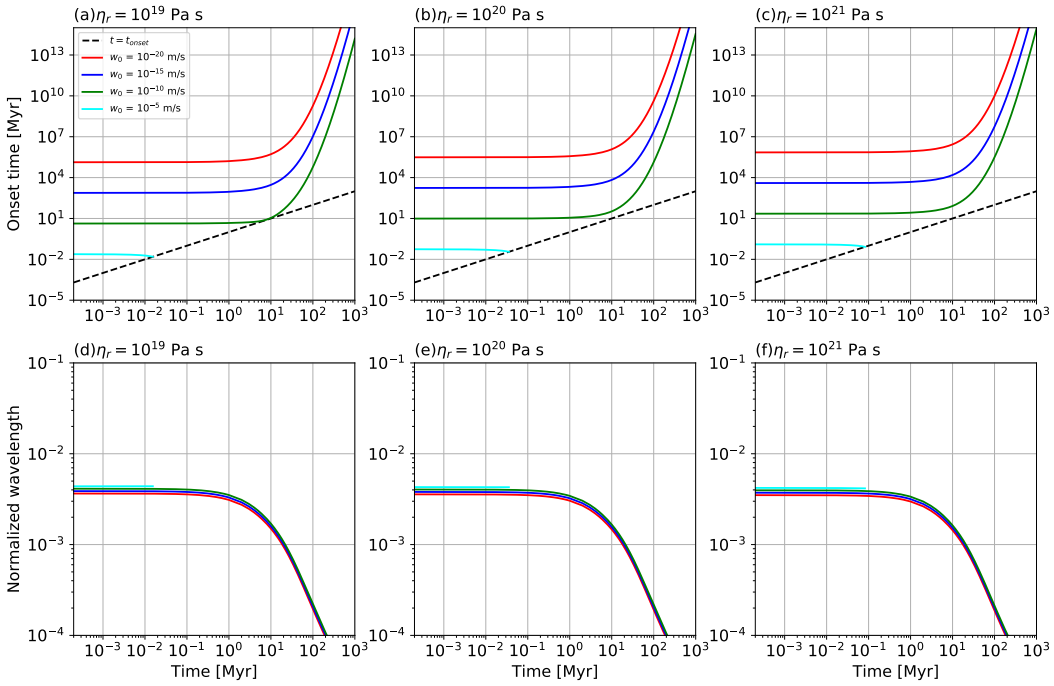

608 **Figure 14.** Time evolution of the onset time (a–c) and normalized wavelength (d–f) for the sinking of the
609 thin IBC layer using the MPG mixing model.

598 Figure 14 shows the evolution of the onset time and normalized wavelength of the
599 overturn for the case of thin IBC layer using the MPG mixing model. For an initial veloc-
600 ity of 10^{-20}–10^{-10} m/s, $t_{\text{onset}} > t$ and the overturn cannot take place. If the initial velocity
601 increases to 10^{-5} m/s, the overturn tends to be possible between $\sim 10^{-2}$ and 10^{-1} Myr.
602 The time evolution of the normalized wavelength is independent of the reference viscosity
603 and initial velocity. For all modelling cases, the normalized overturn wavelength presents
604 a stable value between 10^{-3} and 10^{-2} before $\sim$ 1 Myr and then tends to decrease. For
605 10^{-5} m/s, we observed a numerical breakdown for $t > t_{\text{onset}}$, due to the strong increase of
606 the velocity and of the strain rate as discussed above. In these cases we only plotted the
607 onset time and normalized wavelength until $t = t_{\text{onset}}$.

610 Figure 15 shows the evolution of the onset time and normalized wavelength of the
611 overturn for the case of thick IBC based on the MPG mixing model. For all three ref-
612 erence viscosities, the overturn can occur when the initial velocity reaches 10^{-10} m/s or
613 higher. For all cases, the normalized wavelength is $\sim 10^{-2}$ at the initial time, remains
614 constant, and then decreases from $\sim$ 1 Myr onward. The initial normalized wavelength

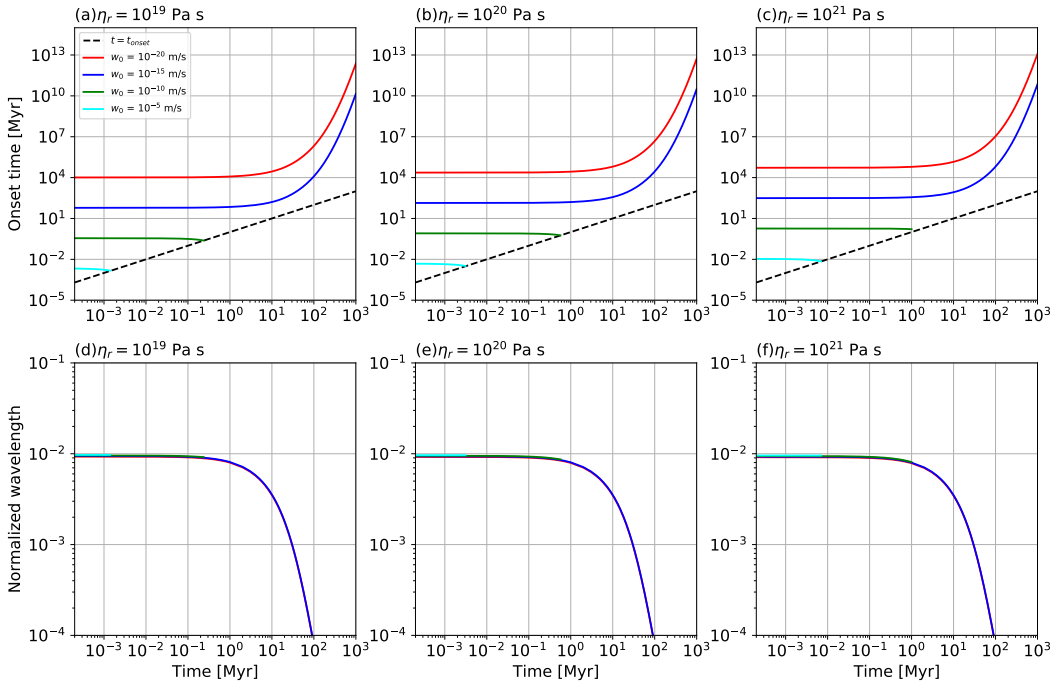

Figure 15. Time evolution of the onset time (a–c) and normalized wavelength (d–f) for the sinking of the thick IBC layer using the MPG mixing model. For the initial velocity of 10^{-10} and 10^{-5} m/s, data are truncated when $t > t_{onset}$ because of the numerical instability relating to the rapidly increasing downwelling velocity.

is slightly shorter than but of the same order with the normalized overturn wavelength of ~ 0.05 when the sinking of thick IBC initiates.

Finally, Figure 16 shows the evolution of the onset time and normalized wavelength of the overturn for the case of thin IBC using the isostress mixing model. Here we just show the results for the initial velocities 10^{-20} and 10^{-15} m/s. The other two initial velocity values always result in a numerical breakdown because of rapidly increasing downwelling velocity. For an initial velocity of 10^{-20}–10^{-15} m/s, the overturn always tends to be possible for $t \leq 1$ Myr unless for an initial velocity of 10^{-20} m/s and a reference viscosity of 10^{21} Pa s. The normalized wavelength varies on the level of $\sim 10^{-2}$ and 10^{-1}, but tends to increase with the increase of initial velocity.

In addition to the geodynamic modelling, Figure 17 shows the evolution of the onset time and normalized wavelength of the overturn for the case of thick IBC using the isostress mixing model. For an initial velocity of 10^{-20}–10^{-15} m/s, the overturn turns out

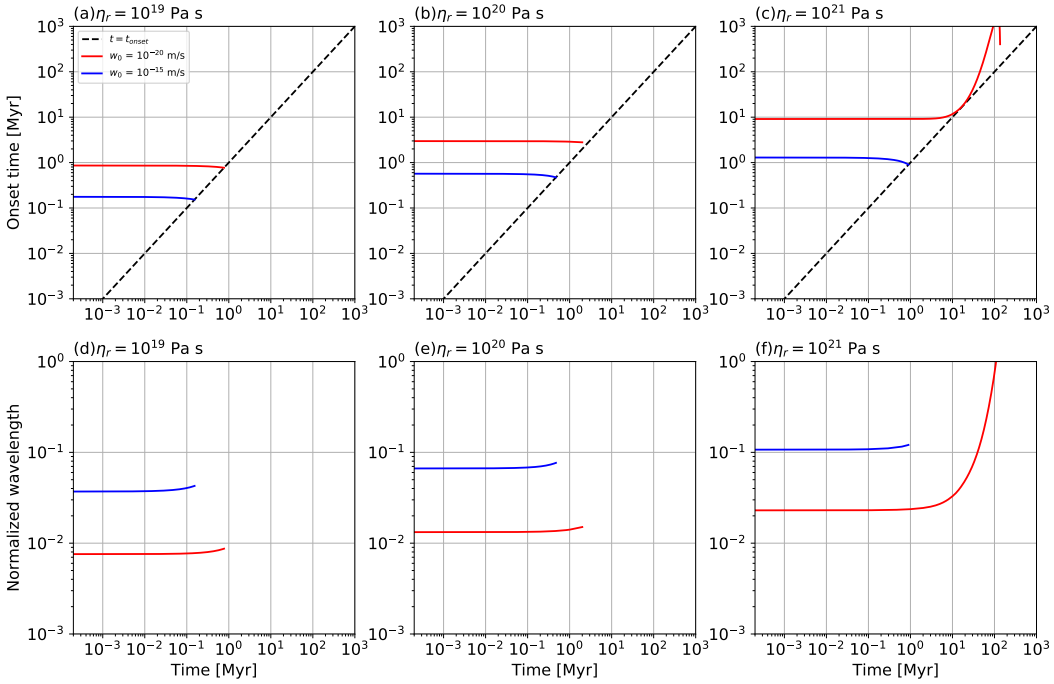

Figure 16. Time evolution of the onset time (a–c) and normalized wavelength (d–f) of the overturn of the case of thin IBC using the isostress mixing model. Data are truncated when $t > t_{onset}$ because of the numerical instability relating to the rapidly increasing downwelling velocity.

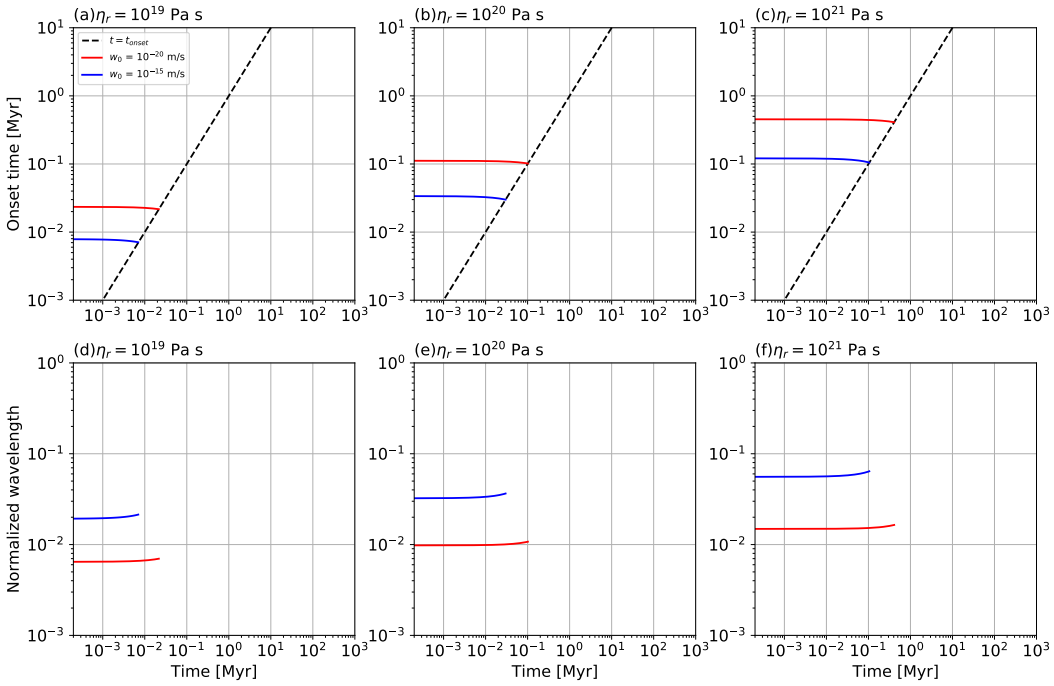

Figure 17. Time evolution of the onset time (a–c) and normalized wavelength (d–f) for the sinking of the thick IBC using the isostress mixing model. Data are truncated when $t > t_{onset}$ because of the numerical instability relating to the rapidly increasing downwelling velocity.

to be possible within the first ~ 1 Myr. The normalized wavelength always shows a value on the level of 10^{-2} and 10^{-1}. Similar to the trend shown in Figure 16, the increase of initial velocity can significantly elongate the overturn wavelength.

5 Discussion

In our previous work we found that under the assumption of diffusion-creep rheology, the sinking of the IBC occurs only for relatively low reference viscosities ($\eta_r \leq 10^{20}$ Pa s) and low activation energies (as low as 100 kJ/mol for $\eta_r = 10^{20}$ Pa s) [*Yu et al.*, 2019]. In particular, we interpreted the need for a low activation energy as indicative of the likely importance of dislocation creep in controlling the overturn [*Christensen*, 1984].

Our models suggest that dislocation creep influences the lunar mantle overturn in a complex way. Although the dislocation creep component provides a viscosity decreasing with the increase of strain rate, whether dislocation creep can promote the overturn or not also depends on the rheological mixing model adopted. Although the dislocation creep

651 tends to dominate the deformation of the IBC layer, the isostrain mixing model does not
652 result in a rheological weakening, but rather in a rheological strengthening of the IBC,
653 which in turn hinders the increase of local strain rate and, accordingly, prevents the IBC
654 from sinking downwards. The MPG mixing model allows a limited rheological weakening
655 of the IBC and correspondingly, a limited increase of the strain rate. In the case of a thin
656 IBC layer, no overturn takes place, while a partial and late overturn is possible when con-
657 sidering a significantly thickened IBC layer. Only the isostress mixing model allows for an
658 early and strong rheological weakening, yielding a rapid and complete overturn.

659 Rheological mixing models are obtained by prescribing partitioning laws for strain
660 rate and stress *a priori*. In reality, their applicability depends on how stress is exerted on
661 each deformable component. The isostrain mixing model corresponds to an axial load-
662 ing for each component, whereas the isostress mixing model corresponds to a transverse
663 loading for each deformable component. These two models provide the upper and lower
664 bound for the effective viscosity of a multiphase rock, respectively. However, they only de-
665 scribe an ideal condition. Whether these two rheological mixing models are applicable for
666 the lunar mantle still need additional experimental verification. The MPG mixing model,
667 which partitions the total strain rate and total stress based on a geometric average under
668 the minimization of viscous dissipation power, does not correspond to a specific loading
669 style. However, based on the summary of *Huet et al.* [2014], this model provides a good
670 approximation for the effective viscosity of multiphase rocks and the partitioning of stress
671 and strain rate among different phases. If the MPG mixing model is also representative for
672 the creep of lunar rocks, our simulations indicate that no overturn would take place in the
673 case of a thin IBC layer. Yet, a partial overturn would occur if newly formed IBC started
674 sinking before the end of magma ocean solidification leading to an effectively thickened
675 IBC layer.

676 Since the growth of ilmenite grains is poorly constrained via experiments, in our
677 models we did not consider dynamic variations of the grain size. These depend on the so-
678 called subgrain rotation and on the attachment of small grains onto larger ones [*Hall and*
679 *Parmentier*, 2003]. The first factor is controlled by the strain rate partitioned through all
680 the dislocation-creep components and results in a reduction of the grain size, whereas the
681 second factor depends on the interfacial energy at the grain boundaries and results in an
682 increase of grain size. *Hall and Parmentier* [2003] modelled the grain size evolution in the
683 framework of mantle convection based on the isostress mixing model. Given typical pa-

rameters for the growth of olivine grains, the models of *Hall and Parmentier* [2003] indicate that the grain size tends to increase over time. Based on Figure 5 and 6, larger solid grains result in a higher reference viscosity, which delays the onset of overturn and enhances the influence of dislocation creep in the IBC. Modelling grain size evolution in the context isostrain and MPG mixing models has received no attention so far. However, for these two rheological mixing models, the increase of IBC strain rate is limited and thus, the effect of subgrain rotation would likely be weaker, while grain growth would be more efficient. For both the MPG and isostrain mixing models, a larger grain size, equivalent to a higher reference viscosity, can retard the onset of overturn and decrease the amount of foundered IBC (see Figure 12).

Based on our Rayleigh-Taylor instability analysis, an increase in the initial downwelling velocity can reduce the onset time of overturn and thus facilitate it. While a high initial velocity shortens the spatial wavelength of the overturn for the isostrain mixing model, it elongates it for the isostress mixing model. For the MPG mixing model, the overturn wavelength is insensitive to the variations of initial velocity.

In our dynamic simulations, we only observed the overturn taking place in long-wavelength structures when using the isostress mixing model. For the thin IBC, the overturn takes place with a normalized wavelength of ~ 0.25. Given that $\lambda \propto D_{\mathrm{IBC}}$, a degree-one overturn could only be possible if the IBC were thickened by a factor of ~ 2, i.e. had a thickness of $\sim$ 72 km, via the small-scale instabilities before complete solidification. Nevertheless, the analysis by the theory of Rayleigh-Taylor instability suggests that elevating the thickness of IBC cannot significantly increase the overturn wavelength (see Figure 16 and 17). When isostress mixing model is exploited, the viscosity of IBC is dominated by the dislocation creep component at the early phase of the overturn. For dislocation creep components, the increase of IBC thickness can also reduce the strain rate in the IBC, which limits the magnitude of viscosity reduction and the elongation of overturn wavelength. Increasing the initial downwelling velocity can effectively elongate the overturn wavelength. However, whether a degree-one overturn can be induced by a high initial downwelling velocity still needs to be verified by improving the numerical techniques of geodynamic modelling for a rapidly-mobilizing IBC. For the likely more realistic MPG mixing model, the overturn wavelength is insensitive to the initial velocity. Hence, the small-scale instabilities observed for MPG model (Figure 8) are probably a robust phenomenon. For the isostrain mixing model, no overturn is possible unless the initial ve-

locity is as high as 10^{-5} m/s. However, increasing the initial velocity causes the overturn wavelength to decrease, leading again to small-scale instabilities, which are then a characteristic of this rheological mixing model.

The initial velocity at the IBC-mantle boundary and the thickness of solidified IBC depend on the shallow mantle dynamics in the solidifying lunar magma ocean. Some investigators suggested that when the new mantle cumulate just forms, the interstitial melt can significantly weaken the local rheology, thus allowing an early onset of the sinking of IBC [e.g. *Parmentier and Hess*, 1999; *Boukaré et al.*, 2018; *Li et al.*, 2019]. Nevertheless, we note that the pre-solidification sinking would be made difficult by the buoyant percolation of interstitial melt, i.e. the melt in the space among the solid grains [e.g. *Solomatov*, 2007]. By using pMELTS to calculate the density of interstitial melt, *Hori and Nagahara* [2015] modelled the time needed for the percolation through the thin mantle cumulate formed in every steps. For a grain size of $\sim$ 1 cm and a porosity of 25–50 vol.%, i.e. the porosity ranging from the closest rhombohedron packing to the most loose cubic packing, interstitial melt may need $\sim$ 10^{-7}–10^{-3} Myr to percolate through the newly formed thin cumulate. As the lunar magma ocean might have lasted up to $\sim$ 200 Myr [e.g. *Elkins-Tanton et al.*, 2011], the percolation of interstitial melts can be treated as a transient process throughout the lunar magma ocean phase. It is still unknown how long the crystallization of IBC has lasted. However, when ilmenite is crystallizing, the co-existing plagioclase can contribute to the thickening of the lunar crust. For a solidifying magma ocean with a growing solid lid atop, the crystallization can significantly be decelerated [*Solomatov*, 2007], thus allowing a sufficiently long time for the interstitial melt to percolate upwards. If this speculation was correct, the dynamics of pre-solidification sinking would finally be dominated by a thin solidified IBC. Based on the theory of Rayleigh-Taylor instability, according to which $t_{\mathrm{onset}} \propto 1/D_{\mathrm{IBC}}$, the pre-solidification sinking may take a considerably long time until the solidified IBC tends to be thick enough near the end of lunar magma ocean crystallization. This speculation is also consistent with an onset of lunar mantle overturn at $\sim$ 4.37 Ga estimated by isotopic chronology [*Sio et al.*, 2020], which is nearly concurrent or slightly earlier than the full solidification of the lunar magma ocean. Based on this analysis, it is questionable whether or not the IBC could be accelerated and thickened sufficiently before the end of lunar magma ocean crystallization. In future works, the overturn will have to be examined in the context of a solidifying lunar magma ocean.

A long-wavelength overturn could also be achieved through the effects of water. Recent studies suggest a water content of ~100 ppm for the bulk Moon [e.g. *Saal et al.*, 2008; *Karato*, 2013]. The water retained in the lunar interior is believed to be indigenous, i.e., to have been attained before the solidification of lunar magma ocean. Otherwise, the rapid formation of the lunar lithosphere would effectively prevent any external sources from delivering water to the deep lunar interior [*Hauri et al.*, 2015]. The detection of water in the lunar exosphere, which hints at an active water cycle, also favours the idea that the Moon is releasing its primordial water [*Benna et al.*, 2019]. On these grounds, a wet lunar magma ocean can be expected. Being highly incompatible, water would concentrate in the upper part of the lunar mantle by the end of magma ocean crystallization, thus further weakening the rheology of IBC. Additionally, the viscosity of clinopyroxene strongly decreases with increasing water content in both diffusion and dislocation creep regimes [*Hier-Ajumder et al.*, 2005; *Chen et al.*, 2006]. As the solidified IBC contain ~ 20–45 vol.% clinopyroxene depending on its thickness (see Section 2.3), the rheology of wet IBC could be further weakened. In future works, the sinking of a hydrous IBC will have to be studied using experimental constraints on the rheologies of wet olivine, clinopyroxene, orthopyroxene, and ilmenite.

6 Conclusions

We evaluated the conditions needed for the mobilization of the IBC layer in the framework of rheologies combining linear diffusion creep and non-linear dislocation creep. When using rheological parameters of dry olivine diffusion-creep, the overturn cannot take place unless the reference viscosity is low enough, i.e. $\eta_r = 10^{19}$ Pa s or lower. Nevertheless, if the sinking of IBC could be initiated before the end of lunar magma ocean solidification, the solidified IBC layer could be thicker. Assuming a thick IBC layer, a partial overturn can always take place for reference viscosities ranging from 10^{19} to 10^{21} Pa s. The influence of dislocation creep on the overturn is not straightforward. Whether or not dislocation creep can promote the overturn crucially depends on the assumed rheological mixing model. The isostrain mixing model causes a rheological strengthening of IBC, which hinders the overturn. The MPG model allows for a limited rheological weakening and can promote a partial overturn in form of small-scale instabilities only in the case of a thick IBC layer. Only the isostress mixing model allows a rapid and complete overturn to take place.

When dislocation creep is considered, the overturn dynamics is also affected by the initial velocity at the IBC-mantle boundary. For all three rheological mixing models, increasing the initial velocity at the IBC-mantle boundary reduces the onset time, which favours the overturn. For the isostrain mixing model, the increase of initial velocity shortens the overturn wavelength, whereas for the isostress mixing model it increases it. For the more realistic MPG mixing model, the overturn wavelength is insensitive to the initial velocity.

One of the hypotheses for the formation of the lunar global asymmetry involves a degree-one overturn. For the isostress mixing model, a degree-one overturn can be promoted by a thickened IBC or a high initial velocity at the IBC-mantle boundary. For the other two rheological mixing models, in particular in the case of the likely more realistic MPG model, the overturn always develops with small-scale instabilities, even upon increasing the initial velocity at the base of IBC layer. Additional rheological weakening due to the presence of water is likely necessary for the development of long-wavelength overturn.

Acknowledgments

S. Yu and L. Xiao were supported by the Science and Technology Development Fund of Macau SAR (121/2017/A3). N. Tosi acknowledge support from the Helmholtz Association (grant VH-NG-1017). N. Tosi and F. Schulz also acknowledge support from the DFG through the priority program SPP-1833 “Building a habitable Earth” (project no. TO 704/2-1). S. Schwinger and D. Breuer were supported by the German Research Foundation (SFB-TRR 170). Computational time was provided by the HLRN (project bep00064), MUST Super-computing Center, which are gratefully acknowledged. We also express our greatest gratitude to the colleagues in Soochow University and Suzhou Super-computing Center (SISCC) for the emergent support of computing services during the outbreak of COVID-2019. The data of this work are shared at https://figshare.com/projects/OverturnWithDislocationCreep/64232.

References

Austin, N. J., and B. Evans (2007), Paleowattmeters: A scaling relation for dynamically recrystallized grain size, *Geology*, *35*(4), 343–346.

Benna, M., D. Hurley, T. Stubbs, P. Mahaffy, and R. Elphic (2019), Lunar soil hydration constrained by exospheric water liberated by meteoroid impacts, *Nature Geoscience*, p. 1.

Boukaré, C.-E., E. Parmentier, and S. Parman (2018), Timing of mantle overturn during magma ocean solidification, *Earth and Planetary Science Letters*, *491*, 216–225.

Boyet, M., R. W. Carlson, L. E. Borg, and M. Horan (2015), Sm–nd systematics of lunar ferroan anorthositic suite rocks: constraints on lunar crust formation, *Geochimica et Cosmochimica Acta*, *148*, 203–218.

Buck, W. R., and M. N. Toksoez (1980), The bulk composition of the moon based on geophysical constraints, in *Proc. Lunar Planet. Sci. Conf.*, vol. 11, pp. 2043–2058.

Bystricky, M., and S. Mackwell (2001), Creep of dry clinopyroxene aggregates, *Journal of Geophysical Research: Solid Earth*, *106*(B7), 13,443–13,454.

Chen, S., T. Hiraga, and D. L. Kohlstedt (2006), Water weakening of clinopyroxene in the dislocation creep regime, *Journal of Geophysical Research Solid Earth*, *111*(B8), –.

Christensen, U. (1984), Convection with pressure-and temperature-dependent non-newtonian rheology, *Geophysical Journal International*, *77*(2), 343–384.

Dygert, N., G. Hirth, and Y. Liang (2016), A flow law for ilmenite in dislocation creep: Implications for lunar cumulate mantle overturn, *Geophysical Research Letters*, *43*(2), 532–540.

Dygert, N. J., R. E. Bernard, and W. M. Behr (2019), Great basin mantle xenoliths record active lithospheric downwelling beneath central nevada, *Geochemistry, Geophysics, Geosystems*, *20*, 751–772, doi:10.1029/2018GC007834.

Elkins-Tanton, L. T., J. A. Van Orman, B. H. Hager, and T. L. Grove (2002), Re-examination of the lunar magma ocean cumulate overturn hypothesis: melting or mixing is required, *Earth and Planetary Science Letters*, *196*(3), 239–249.

Elkins-Tanton, L. T., S. Burgess, and Q.-Z. Yin (2011), The lunar magma ocean: Reconciling the solidification process with lunar petrology and geochronology, *Earth and Planetary Science Letters*, *304*, 326–336.

Garcia, R., J. Gagnepain-Beyneix, S. Chevrot, and P. Lognonné (2011), Very preliminary reference moon model, *Physics of the Earth and Planetary Interiors*, *188*(1–2), 96–113.

Ghiorso, M. S., M. M. Hirschmann, P. W. Reiners, and V. C. Kress (2002), The pmelts: A revision of melts for improved calculation of phase relations and major element partitioning related to partial melting of the mantle to 3 gpa, *Geochemistry, Geophysics,*

Geosystems, *3*(5), 1–36.

Hall, C. E., and E. Parmentier (2003), Influence of grain size evolution on convective instability, *Geochemistry, Geophysics, Geosystems*, *4*(3).

Harada, Y., S. Goossens, K. Matsumoto, J. Yan, J. Ping, H. Noda, and J. Haruyama (2014), Strong tidal heating in an ultralow-viscosity zone at the core–mantle boundary of the moon, *Nature Geoscience*, *7*, 569–572, doi:10.1038/ngeo2211.

Haskin, L. A., R. L. Korotev, K. M. Rockow, and B. L. Jolliff (1998), The case for an imbrium origin of the apollo thorium-rich impact-melt breccias, *Meteoritics and Planetary Science*, *33*(5), 959–975.

Hauri, E. H., A. E. Saal, M. J. Rutherford, and J. A. V. Orman (2015), Water in the moon's interior: Truth and consequences, *Earth and Planetary Science Letters*, *409*, 252–264.

Hess, P., and E. Parmentier (1995), A model for the thermal and chemical evolution of the moon's interior: Implications for the onset of mare volcanism, *Earth and Planetary Science Letters*, *134*(3), 501–514.

Hier-Ajumder, S., S. Mei, and D. L. Kohlstedt (2005), Water weakening of clinopyroxenite in diffusion creep, *Journal of Geophysical Research Solid Earth*, *110*(110), 542–557.

Hirth, G., and D. Kohlstedt (2003), *Rheology of the Upper Mantle and the Mantle Wedge: A View from the Experimentalists*, 83-105 pp., American Geophysical Union.

Hori, A., and H. Nagahara (2015), The role of melt percolation on differentiation of lunar magma ocean, in *Lunar and Planetary Science Conference*, vol. 46, p. 2381.

Houseman, G. A., and P. Molnar (1997), Gravitational (rayleigh–taylor) instability of a layer with non-linear viscosity and convective thinning of continental lithosphere, *Geophysical Journal International*, *128*(1), 125–150.

Huet, B., P. Yamato, and B. Grasemann (2014), The minimized power geometric model: An analytical mixing model for calculating polyphase rock viscosities consistent with experimental data, *Journal of Geophysical Research: Solid Earth*, *119*(4), 3897–3924.

Hüttig, C., N. Tosi, and W. B. Moore (2013), An improved formulation of the incompressible navier–stokes equations with variable viscosity, *Physics of the Earth and Planetary Interiors*, *220*(4), 11–18.

Jolliff, B. L., J. J. Gillis, L. A. Haskin, R. L. Korotev, and M. A. Wieczorek (2000), Major lunar crustal terranes: Surface expressions and crust-mantle origins, *Journal of Geophysical Research: Planets (1991–2012)*, *105*(E2), 4197–4216.

878 Karato, S., and P. Wu (1993), Rheology of the upper mantle: a synthesis, *Science*,
879 *260*(5109), 771–8.

880 Karato, S. I. (2013), Geophysical constraints on the water content of the lunar mantle
881 and its implications for the origin of the moon, *Earth and Planetary Science Letters*,
882 *384*(13), 144–153.

883 Korotev, R. L. (2000), The great lunar hot spot and the composition and origin of the
884 apollo mafic ("lkfm") impact-melt breccias, *Journal of Geophysical Research: Planets*
885 *(1991–2012)*, *105*(E2), 4317–4345.

886 Laneuville, M., M. A. Wieczorek, D. Breuer, J. Aubert, G. Morard, and T. Rückriemen
887 (2014), A long-lived lunar dynamo powered by core crystallization, *Earth and Planetary*
888 *Science Letters*, *401*(401), 251–260.

889 Li, H., N. Zhang, Y. Liang, B. Wu, N. J. Dygert, J. Huang, and E. Parmentier (2019), Lu-
890 nar cumulate mantle overturn: A model constrained by ilmenite rheology, *Journal of*
891 *Geophysical Research: Planets*.

892 Mackwell, S. J. (1991), High-temperature rheology of enstatite: Implications for creep in
893 the mantle, *Geophysical Research Letters*, *18*(11), 2027–2030.

894 Maurice, M., N. Tosi, H. Samuel, A.-C. Plesa, C. Hüttig, and D. Breuer (2017), Onset of
895 solid-state mantle convection and mixing during magma ocean solidification, *Journal of*
896 *Geophysical Research (Planets)*, *122*(3), 577–598, doi:10.1002/2016JE005250.

897 Molnar, P., G. A. Houseman, and C. P. Conrad (1998), Rayleigh—taylor instability and
898 convective thinning of mechanically thickened lithosphere: effects of non-linear vis-
899 cosity decreasing exponentially with depth and of horizontal shortening of the layer,
900 *Geophysical Journal International*, *133*(3), 568–584.

901 Morgan, J. W., J. Hertogen, and E. Anders (1978), The moon: Composition determined by
902 nebular processes, *Moon and the Planets*, *18*(4), 465–478.

903 Nimmo, F., U. H. Faul, and E. J. Garnero (2012), Dissipation at tidal and seismic frequen-
904 cies in a melt-free Moon, *Journal of Geophysical Research: Planets*, *117*, E09005, doi:
905 10.1029/2012JE004160.

906 O'Neill, H. S. C. (1991), The origin of the Moon and the early history of the Earth – A
907 chemical model. Part 1: The moon, *Geochimica et Cosmochimica Acta*, *55:4*(4), 1159–
908 1172.

909 Parmentier, E., and P. Hess (1999), On the chemical differentiation and subsequent evolu-
910 tion of the moon, in *Lunar and Planetary Science Conference*, vol. 30.

Parmentier, E., S. Zhong, and M. Zuber (2002), Gravitational differentiation due to initial chemical stratification: origin of lunar asymmetry by the creep of dense kreep?, *Earth and Planetary Science Letters*, *201*(3), 473–480.

Plesa, A.-C., N. Tosi, and C. Hüttig (2012), Thermochemical convection in planetary mantles: advection methods and magma ocean overturn simulations, in *Integrated Information and Computing Systems for Natural, Spatial, and Social Sciences*, edited by C.-P. Rueckemann, pp. 302–323, IGI Global, doi:10.4018/978-1-4666-2190-9.ch015.

Rozel, A., Y. Ricard, and D. Bercovici (2011), A thermodynamically self-consistent damage equation for grain size evolution during dynamic recrystallization, *Geophysical Journal International*, *184*(2), 719–728.

Saal, A. E., E. H. Hauri, M. L. Cascio, J. A. V. Orman, M. C. Rutherford, and R. F. Cooper (2008), Volatile content of lunar volcanic glasses and the presence of water in the moon's interior, *Nature*, *454*(7201), 192.

Schubert, G., D. L. Turcotte, and P. Olson (2001), *Mantle Convection in the Earth and Planets, Part 1*, vol. 940, 956 pp.

Schulz, F., N. Tosi, A.-C. Plesa, and D. Breuer (2020), Stagnant-lid convection with diffusion and dislocation creep rheology: Influence of a non-evolving grain size, *Geophysical Journal International*, *220*(1), 18–36, doi:10.1093/gji/ggz417.

Shea, E. K., and M. D. Fuller (2012), A long-lived lunar core dynamo., *Science*, *335*(6067), 453–6.

Sio, C. K., L. E. Borg, and W. S. Cassata (2020), The timing of lunar solidification and mantle overturn recorded in ferroan anorthosite 62237, *Earth and Planetary Science Letters*, *538*, 116,219.

Smith, P. M., and P. D. Asimow (2005), Adiabat_1ph: A new public front-end to the MELTS, pMELTS, and pHMELTS models, *Geochemistry, Geophysics, Geosystems*, *6*(2), doi:10.1029/2004GC000816.

Snyder, G. A., L. A. Taylor, and C. R. Neal (1992), A chemical model for generating the sources of mare basalts: Combined equilibrium and fractional crystallization of the lunar magmasphere, *Geochimica et Cosmochimica Acta*, *56*(10), 3809–3823.

Solomatov, V. S. (2007), Magma oceans and primordial mantle differentiation, *Treatise on geophysics*, *9*, 91–120.

Stegman, D. R., M. A. Jellinek, S. A. Zatman, J. R. Baumgardner, and M. A. Richards (2003), An early lunar core dynamo driven by thermochemical mantle convection, *Na-*

ture, *421*, 143–146.

Tasaka, M., T. Hiraga, and M. E. Zimmerman (2013), Influence of mineral fraction on the rheological properties of forsteriteâĂĽ+ enstatite during grainâĂŘsizeâĂŘsensitive creep: 2. deformation experiments, *Journal of Geophysical Research Solid Earth*, *118*(8), 3991–4012.

Till, J. L., and B. Moskowitz (2013), Magnetite deformation mechanism maps for better prediction of strain partitioning, *Geophysical Research Letters*, *40*(4), 697–702, doi:10.1002/grl.50170.

Tullis, T. E., F. G. Horowitz, and J. Tullis (1991), Flow laws of polyphase aggregates from end-member flow laws, *Journal of Geophysical Research: Solid Earth*, *96*(B5), 8081–8096.

Viswanathan, V., N. Rambaux, A. Fienga, J. Laskar, and M. Gastineau (2019), Observational constraint on the radius and oblateness of the lunar core-mantle boundary, *Geophysical Research Letters*, *46*(13), 7295–7303.

Weber, R. C., P.-Y. Lin, E. J. Garnero, Q. Williams, and P. Lognonné (2011), Seismic detection of the lunar core, *Science*, *331*(6015), 309–312.

Whitehead, J. A. (1988), Fluid models of geological hotspots, *Annual Review of Fluid Mechanics*, *20*(20), 61–87.

Wieczorek, M. A., and R. J. Phillips (2000), The "procellarum kreep terrane": Implications for mare volcanism and lunar evolution, *Journal of Geophysical Research: Planets (1991–2012)*, *105*(E8), 20,417–20,430.

Yu, S., N. Tosi, S. Schwinger, M. Maurice, D. Breuer, and L. Xiao (2019), Overturn of ilmenite-bearing cumulates in a rheologically weak lunar mantle, *Journal of Geophysical Research: Planets*, *124*(2), 418–436.

Zhang, N., E. M. Parmentier, and Y. Liang (2013), A 3-d numerical study of the thermal evolution of the moon after cumulate mantle overturn: the importance of rheology and core solidification, *Journal of Geophysical Research: Planets*, *118*, 1789–1804, doi:10.1002/jgre.20121.

Zhao, Y., J. de Vries, A. van den Berg, M. Jacobs, and W. van Westrenen (2019), The participation of ilmenite-bearing cumulates in lunar mantle overturn, *Earth and Planetary Science Letters*, *511*, 1–11.

Zhong, S., E. M. Parmentier, and M. T. Zuber (2000), A dynamic origin for the global asymmetry of lunar mare basalts, *Earth and Planetary Science Letters*, *177*(3), 131–140.